AN ABSTRACT OF THE THESIS OF

Alexandra Joyce Simpson for the degree of Master of Science in Civil Engineering presented on September 1, 2016.

Title: Wave-by-Wave Forecasting via Assimilation of Marine Radar Data

Abstract approved:

_____

Merrick C. Haller

A wave-by-wave forecasting system is desired for optimization of wave energy conversion devices and for improving safety of vessel-based marine operations. This study outlines the first validation attempts of a recently developed forecasting system called Wavecast. The forecasting approach uses X-Band marine radar images for data assimilation, then reconstructs and propagates the ocean wave field in both space and time using the Mild Slope Equation wave model. For data assimilation, the radial component of the sea surface slope is computed from the radar imagery using the recently-derived Radar Model (Lyzenga & Walker, 2015). The Radar Model is a direct relationship between radar backscatter intensity and radial slope, without the need for external calibration. Validation attempts of the forecasting system are carried out in two phases. First, synthetic data is used. Two trials are presented: a simple monochromatic dataset, and a nonlinear simulation of a realistic sea. Results of monochromatic testing show strong spectral correlation, and time series correlation of up to 0.9 throughout the full domain. Results of nonlinear testing show up to 83% spectral correlation of significant wave height, time series correlation up to 0.9 among reconstructed waves, but some decay in correlation among predicted waves. Next a field dataset is presented, which was collected by a ship-mounted radar offshore Newport, OR with spatial and temporal overlap to a TRIAXYS wave profiling buoy. The field dataset provides several challenges. Noise in the electronic compass readings prevented rectification of the ship's motion; however, this was overcome using a novel post-processing technique on the radar images to georeference each scan without the need for electronic compass readings. Additionally, uncertainty exists in the location of the TRIAXYS buoy; thus, a cross-correlation analysis was performed on a small region surrounding the buoy's anticipated location to determine the location of maximum correlation between actual and model time series. Despite complexities in the field dataset, assimilation of the field data in Wavecast shows good spectral reconstruction, with issues remaining in time series correlation. The presented validation attempts provide improved understanding of the accuracy and potential of Wavecast, and give support for the validity of the Radar Model.

©Copyright by Alexandra Joyce Simpson
September 1, 2016
All Rights Reserved

Wave-by-Wave Forecasting via Assimilation of Marine Radar Data

by
Alexandra Joyce Simpson

A THESIS

submitted to

Oregon State University

in partial fulfillment of
the requirements for the
degree of

Master of Science

Presented September 1, 2016
Commencement June 2017

Master of Science thesis of Alexandra Joyce Simpson presented on September 1, 2016

APPROVED:

Major Professor, representing Civil Engineering

Head of the School of Civil and Construction Engineering

Dean of the Graduate School

I understand that my thesis will become part of the permanent collection of Oregon State University libraries. My signature below authorizes release of my thesis to any reader upon request.

Alexandra Joyce Simpson, Author

ACKNOWLEDGEMENTS

To my advisor, Merrick Haller, I'm grateful for your unending guidance and patience. Working with you has helped me to mature as a scientist and as a person. Thank you for respecting my ideas, for leading me towards lessons before answers, and for always finding the best illustrative metaphors for the tough concepts.

There are numerous other mentors I would like to acknowledge. To my committee members, Tuba Özkan-Haller, Ted Brekken and Geoff Hollinger, thank you for being engaged in this work and for providing your feedback. To David Honegger and Randy Pittman, I'm so appreciative of your help in all things computers and radar, especially related to the collection and post processing of our field dataset. Thank you to the members of the Coastal Engineering faculty for your encouraging conversations and dedication to teaching. I would also like to thank everyone I've worked with in NNMREC for continuing to engage me in the field of marine renewable energy.

To the friends I've made the past two years, you've been irreplaceable sources of happiness and stability. Thank you for the non-academic lessons you've taught me, and the many weekends you've rallied me on outdoor adventures. To the friends I've also had the privilege of calling classmates, your intellectual curiosity is profoundly inspiring. It will be an honor to consider you colleagues. To my parents, it is the greatest gift to always have you on my team. And to Amie, thank you for continuing to join me on this journey.

This work was supported by award number DE-EE0006789 through the Energy Efficiency and Renewable Energy Program of the US Department of Energy. Thank you to NNMREC for providing access to the TRIAXYS directional wave buoy, and to the Umatilla II for support in field data collection. I would also like to acknowledge our team members David Walker, Dean Jordan and Patrick Lynett for providing us with Wavecast, and continuous support along the way.

TABLE OF CONTENTS

Page

LIST OF FIGURES

LIST OF TABLES

Table Page

An Introduction to Wave-by-Wave Forecasting

Wave-by-wave forecasting (also known as "phase-resolved" wave forecasting) is the process by which the time-varying water surface elevation over a spatial domain is predicted. Differing from forecasts of bulk wave parameters, where predictions are typically made on time scales of hours to days, wave-by-wave forecasts are made on a much shorter time scale, typically of seconds to minutes with sub-second time resolution. There are many motivations for an accurate, real-time method of wave-by-wave forecasting. Offshore operations such as cargo transfer, helicopter landing, and vessel positioning would benefit from the prediction of workable time windows or large wave warnings (Borge et al., 2004; Naaijen & Wijaya, 2014; Wijaya et al., 2015). An additional, active area of research for applications of such a system is the optimization and control of Wave Energy Conversion (WEC) devices in order to improve their efficiency.

A WEC harnesses energy by oscillating with ocean waves. To oscillate optimally, various control strategies have been proposed which tune the WEC to the wave field. In monochromatic waves, the tuning system would look much like a simple damped mass-spring duo, forcing the natural period of the device to the period of the wave (Budal & Falnes, 1982). Of course, in real seas, waves are much more complex. An implementable control strategy will require accurate knowledge of the incoming wave field to tune some aspect of the WEC's behavior. Tuning can be achieved by passively adjusting the device's power take off to forecasts of statistical parameters, such as significant wave height. The resulting control strategy would improve performance on time scales of the forecasted parameter, however maximum energy extraction would only be achieved from a small fraction of the waves it experienced. A much more effective technique is to tune the WEC on a wave-by-wave basis by utilizing a phase-resolved wave forecast of several wave periods. Such a control strategy will optimize energy capture from most or all waves, as well as improve device survivability in extreme conditions (Brekken, 2011; Fusco & Ringwood, 2010a). While considerable research has been devoted to developing these strategies, a gap still remains in the ability to provide a wave-by-wave forecast. Should an effective wave-by-wave forecasting technique be developed, it will be a key component of WEC optimization techniques, and an influential development for the advancement of the industry.

For effective controlling, forecast length requirements vary throughout the literature from several seconds to a minute (Brekken, 2011; Fusco & Ringwood, 2012; Li et al., 2012). There are two main approaches to forecasting that have been proposed. One method aims to make a prediction at the WEC location using a purely mathematical model. The idea is to record surface elevation or excitation forces using the WEC itself, and predict into the future based on this record. This scheme is demonstrated in Figure 1 (a). The main proposed approaches include decomposition of the signal into its frequency components (Halliday et al., 2011), and autoregressive methods such as linear auto

regression and neural networks (Fusco & Ringwood, 2010a, 2010b; Schoen et al., 2011). Forecasting based on mathematical models has been shown to work for one to two wave periods, but beyond that the accuracy of the forecast tends to break down. The competing idea is demonstrated in Figure 1 (b). Often referred to as Deterministic Sea Wave Prediction (DSWP), this idea is to observe the sea surface surrounding a WEC device, then use a wave model to reconstruct and predict the wave field forward in space and time. If the modeled waves can be propagated to the WEC faster than the actual waves, a forecast can be made.

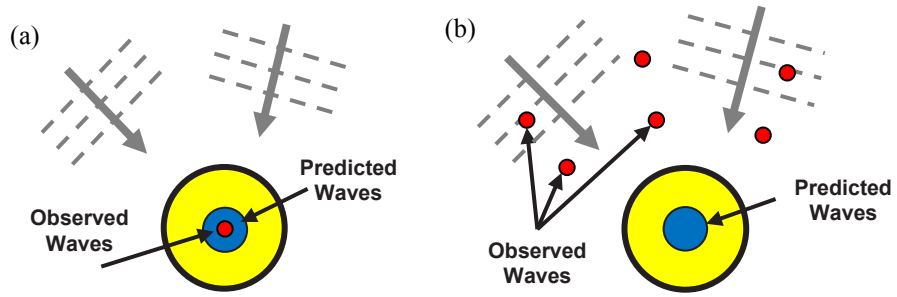

Figure 1. Two main approaches to wave-by-wave forecasting, based on Fusco & Ringwood (2010a): (a) Prediction in time using wave record at point location and (b) Prediction in space and time using a reconstruction of the wave field.

The presented work uses the latter approach. DSWP is a relatively new area of research with limited literature, the majority of which is designed for vessel-based applications. While some work has been undertaken on the prediction of nonlinear waves (Blondel et al., 2008; Wu, 2004; Zhang et al., 1999), computation time has exceeded the possibility of utilizing such approaches in real-time, with little gain in accuracy. For practical application, the focus in the literature has been on linear wave models (Belmont et al., 2014; Belmont et al., 2006; Belmont et al., 2003). Since many applications are for marine operations, DSWP methods are often focused on the prediction of quiescent intervals (Belmont et al., 2014; Belmont, et al., 2006). Knowledge of these intervals may be sufficient for nautical applications such as cargo transfer and helicopter landing, however for WEC applications, a more exact wave-by-wave forecast is desired.

In DSWP, observations throughout the sea surface must be acquired for input to the wave model. There are two proposed techniques for collecting these observations: wave buoys that record water surface elevation time series at discrete points throughout the wave field, or remote sensing, which is essentially like taking thousands of discrete observations throughout a 2D domain. Using a small number of discrete number of observations in DSWP has been shown to present challenges in multi-directional seas (Belmont et al., 2014; Janssen et al., 2001). Additionally, For WEC applications, the deployment of numerous wave measurement buoys can be costly, and transmission of wave

information to the device presents an added operational challenge. In maritime applications, the motion of the vessel obviates the use of wave buoys.

Thus, an effective remote sensing technique is desired. At present, satellites cannot provide the spatial or temporal resolution needed for real-time forecasting. Lidar has been proposed as well, but is most effective for sea surface observations when operated at large grazing angles, thus limiting the observation range. Techniques using low grazing angles are effective when observing bores, but the surface of non-breaking waves tends to absorb the optical beam rather than reflect it (Belmont et al., 2008). A more plausible option is the marine radar, as it is well known for its ability to image ocean waves through modulations of backscatter intensity. Radar is an attractive remote sensing tool because of its existing widespread nautical use, its relatively low cost, and its large spatial resolution.

We have developed a DSWP method that we call "Wavecast" which couples a marine radar with a linear wave model for reconstruction and prediction of the remotely sensed waves. The backbone of Wavecast is shown in Figure 1.

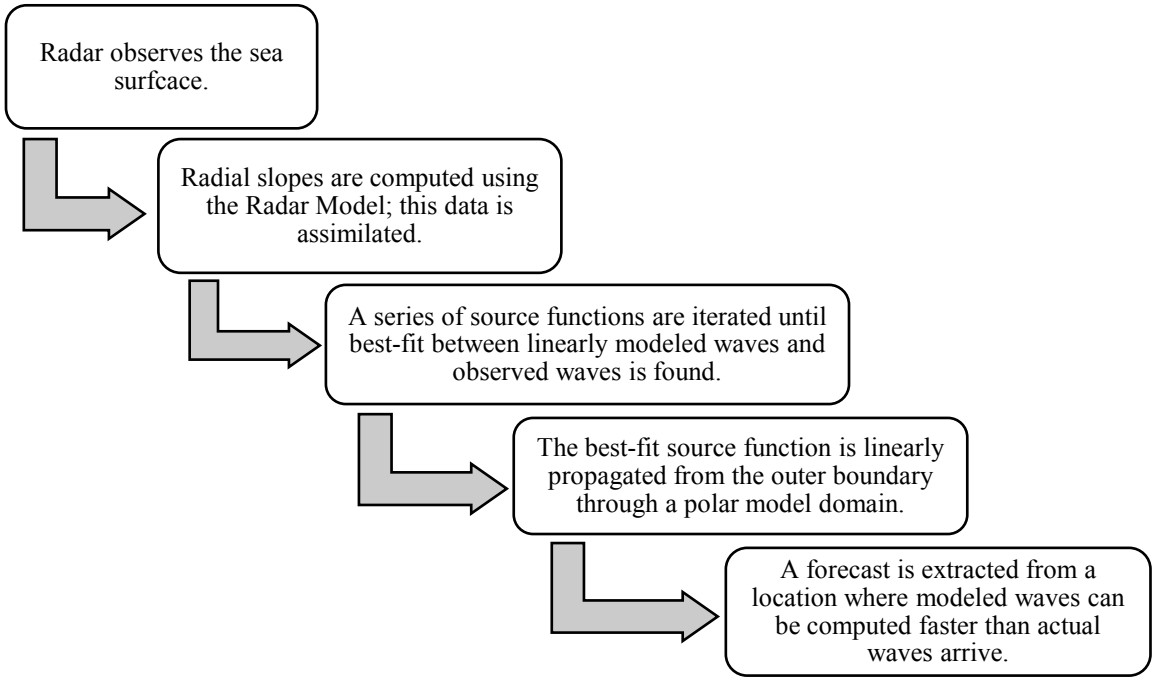

Figure 2. Structure of the Wavecast system.

The ability to directly and robustly retrieve wave information from radar imagery is an ongoing area of research. It is a challenging problem because the mechanisms that modulate the radar signal are complex and difficult to mathematically model. Various proposed techniques for reconstruction of waves from radar imagery are discussed in the introduction of the manuscript. In the Wavecast system, we use a recently derived relationship between the radar backscatter intensity, and the radial component of surface slope, which we call the "Radar Model."

The presented manuscript outlines our validation attempts of the Wavecast system. Through use of a synthetic radial slope dataset, Wavecast is first validated without the implementation of the Radar Model. Then, a field dataset is used in the complete Wavecast system, allowing for validation of the Radar Model as well. The synthetic dataset is a wave field computed using a nonlinear Boussinesq model in a polar domain. From the synthetic surface elevations, radial slope has been computed using a finite differencing approach. Field validation was conducted using a dataset comprised of radar scans and surface elevation measurements that overlap in time and space, collected offshore Newport, Oregon in December 2015. The radar data was collected by mounting the radar onboard the Umatilla II, a charter fishing vessel, and positioning the vessel in proximity to a TRIAXYS wave profiling buoy. The TRIAXYS is owned and operated by the Northwest National Marine Renewable Energy Center, and throughout data collection was moored in the South Energy Test Site (SETS). This site is anticipated for full-scale, grid-connected testing of WEC devices, chosen for its promising resource of wave energy. Conducting our field testing of Wavecast within the SETS site allows for validation in conditions anticipated for WEC operation.

A Wave-by-Wave Forecasting System via Data Assimilation of Marine Radar Images

Alexandra J. Simpson
Oregon State University, Corvallis, Oregon

Merrick C. Haller
Oregon State University, Corvallis, Oregon

David Walker
SRI International, Ann Arbor, Michigan

Patrick Lynett
University of Southern California, Los Angeles, California

Journal: *American Meteorological Society*
Journal of Atmospheric and Oceanic Technology

45 Beacon Street
Boston, MA 02108-3693

To be submitted 2016

Abstract

Herein a phase-resolving wave forecasting system that couples radar data assimilation with wave field reconstruction and forward prediction is presented. Wave information is extracted from the radar image time series using a recently derived relationship between the radar backscatter intensity and the radial component of the sea surface slope. The developed forecast algorithm assimilates the radar-derived radial slope information, which is coupled with the Mild Slope Equation (MSE) to compute a hindcast of wavemaker source conditions that produced the observed waves. These source conditions are propagated using the MSE across a polar domain in faster than real time to acquire a forecast at a desired point location some distance inside of the outer boundary. The system undergoes synthetic validation, and preliminary in-field validation using a dataset collected offshore Newport, OR.

1. Introduction

A real-time wave-by-wave forecasting system has been highly sought after for use in ship operations, and for the optimization of wave energy conversion (WEC) devices. For maritime applications, tasks such as cargo transfer, helicopter landing, and vessel positioning would benefit from the prediction of workable time windows or freak waves (Belmont et al., 2014; Borge et al., 2004; Naaijen & Wijaya, 2014). For WECs, the amount of extractable energy can be significantly improved when the device's behavior is tuned on a wave-by-wave basis (Belmont et al., 2014; Brekken, 2011; Fusco & Ringwood, 2010a; Li et al., 2012). In this study, we present a method for wave-by-wave forecasting that couples the Mild Slope Equation wave model with a novel method of extracting the radial component of sea surface slope from radar imagery.

It has long been known that ocean waves are visible in marine radar images. The dominant interaction between radar electromagnetic waves and the sea surface is Bragg scattering, by which only water waves of wavenumber $2\,k\sin\theta$ contribute to radar backscatter. Longer gravity waves are visible when this interaction with surface ripples is modulated. Three modulation mechanisms dominate: (1) hydrodynamic modulation, in which the surface Bragg-scattering ripples interact with the longer gravity waves, (2) tilt modulation, in which the effective incidence angle of the radar is affected by the gravity wave slope, and (3) shadowing, in which areas behind a gravity wave are not being directly measured by the radar signal (Borge et al., 2004). Because of the complexity of these mechanisms and their interactions, geophysical parameters of the sea surface are not easily extracted from the radar backscatter intensity.

Attempts to retrieve wave information from radar data dates back to the 1960's, in which radar images were inspected visually to obtain estimates of wave direction, wave length and period (Ijima et

al., 1964; Wright, 1965). Since, notable improvements have been made in quantifying wave spectra for retrieval of statistical wave parameters (Borge et al., 1999; Ziemer & Gunther, 1994). Additional studies have shown that radar is capable of resolving bathymetry and surface currents (Senet et al., 2001; Young et al., 1985). It is only within recent years that radar has been investigated for phase-resolved wave field measurements.

The majority of sea surface reconstruction attempts use a method that considers shadowing the dominant imaging mechanism. Three-dimensional Fourier analysis is used to create a spectral representation of the radar images (Young et al., 1985), from which signals satisfying the linear dispersion relationship can be extracted. This dispersion filtered spectra is close in shape to the actual wave spectra, and may be scaled using an external calibration factor so that it matches in magnitude as well (Borge et al., 2004; Qi et al., 2016). The calibration factor has been typically solved for empirically, and can be problematic in its accuracy and versatility.

Alternatively, methods have been introduced that use surface tilt as the dominant imaging mechanism (Dankert & Rosenthal, 2004). This technique ignores shadowing effects, which is limiting in the allowable grazing angle of the radar; it must be large enough to not induce significant shadowing throughout the image domain. However, a major benefit of using surface tilt models is that external calibration is not needed. The proposed study uses a reconstruction technique referred to as the "Radar Model" that is built on a surface tilt model, but additionally accounts for geometric shadowing effects. The result is a direct relationship between the radial slope of ocean waves and the radar backscatter intensity, applicable in low grazing angles and without the need for external calibration. Derived recently by Lyzenga and Walker (2015), the Radar Model is applied for the first time in this study to compute radial slope for assimilation into a forecasting algorithm.

The developed forecasting algorithm, which we refer to as Wavecast, couples the Radar Model with a novel assimilation and prediction routine. Wavecast uses a model domain in polar coordinates for compatibility with the radar images. The Mild Slope Equation wave model is used to produce a wavemaker source function along the outer range of the boundary. The best-fit source function is determined through minimization of a cost function, which is iterated until the modeled waves match the radar-observed waves. When the best-fit source function has been found, the waves are propagated through the polar domain towards the origin. By computing these waves in faster than real time, a forecast is made before the actual waves arrive.

In Section 2 of this paper, the structure of the Wavecast algorithm is outlined. In Section 3, the derivation of the Radar Model is briefly explained, including a discussion of the assumptions involved. In Section 4, synthetic validation of the Wavecast algorithm is provided. The synthetic data is a time

series of radial slope computed using both monochromatic waves and a weakly nonlinear Boussinesq model of surface elevation. By using synthetic input data, the step requiring the Radar Model can be bypassed. Section 5 approaches the validation using a field dataset collected offshore Newport, OR, which allows for validation of Wavecast incorporating the Radar Model. The forecasted waves are compared to in situ data collected by a TRIAXYS wave profiling buoy. Section 6 provides a technique for improving the accuracy of wave phase speed, whereby the input source functions are filtered to a narrower bandwidth than initial Wavecast runs. Discussion of the constraints to forecasting in real-time is provided in Section 7. Summary and conclusions are given in Section 8.

2. Wavecast

2.1 Model Domain

The Wavecast model domain is defined in polar coordinates for compatibility with the radar data. A schematic of the polar model domain is shown in Figure 3. The gray gridlines are a coarsened representation of the typical model resolution, where each range line represents 50 indices (150 m) and each azimuth line represents 7 indices (5 degrees). The region outlined in blue is the annulus of radar data used for assimilation. Sponge layers are drawn as red dashed lines inside of the outer bounds of the computation domain, used for minimizing reflection off the boundary walls. The source function is applied at the sponge layer range inside of the assimilation domain, and the waves are propagated across the computation domain towards the origin. As the waves leave the assimilation region, they are no longer waves that have been reconstructed from input data, and thus are predicted waves.

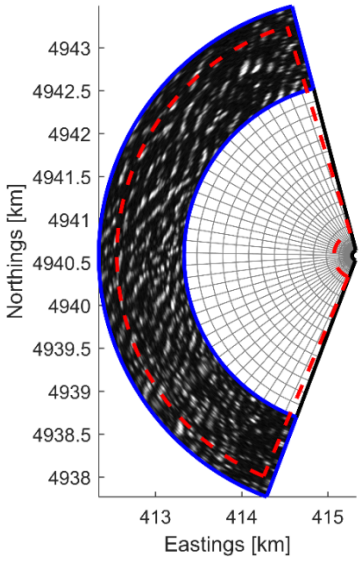

Figure 3. Schematic of the Wavecast polar computation domain.

2.2 Data Assimilation

Radar images are collected for use as data assimilation. The raw radar images are processed using the Radar Model, to be described in Section 3. The Radar Model converts the raw intensity values into the radial component of the sea surface slope, which is the data used for assimilation in the Wavecast system.

In an operational use of Wavecast, the entire scan of observations collected by the radar will not be used for assimilation; only an annulus at the outermost range of the grid is used. This is because the larger the region of data input, the longer the computation time. Thus, the size of the annulus of data used for assimilation must be chosen consciously, to balance accuracy with computation cost. Using too small of an annulus will result in poor reconstruction of the wave field. Using too large of an annulus will reduce the duration of prediction. Throughout the model runs presented in this manuscript, the width of the assimilation annulus spans between spans between 800–2000 meters (approx. 5–12 wavelengths). For initial testing of the model, optimization of the size of this annulus has not yet been considered.

An additional consideration in choosing the region for data assimilation is the location of the annulus within the radar domain. First and foremost, the annulus must be oriented so that it contains waves travelling towards the radar. Only waves in the up-wave direction can be used, as the model propagates waves from the outermost boundary towards the radar. An additional consideration that must be made is the chosen range of the annulus. The amount of shadowing and level of noise in the radar images increases with range. Thus, making the annulus too far from the radar will lead to assimilation of poor quality data. However, choosing the annulus too close to the radar will limit the possible size of the computation domain. The larger the computation domain, the longer Wavecast has to compute the model waves before the actual waves arrive.

2.3 Estimating the Source Function

From the assimilated data, a best-fit source function is computed using the Mild Slope Equation wave model. The source function is the time series of water surface elevation along the inner edge of the sponge layer at the outer edge of the domain. It is used to initialize the waves that are sent through the model domain, essentially acting like a wavemaker. The source function is included as the term *S* in the Mild Slope Equations:

$$\eta_t = -\nabla \cdot (CC_g \nabla \phi) + (\omega^2 - k^2 CC_g)\phi + S$$

$$\phi_t = -\eta,$$

In the MSEs, the first equation solves for the water surface elevation η, and the second solves for the velocity potential ϕ, using knowledge of the wave speed C, wave group speed C_g, and wavenumber k all as a function of position for a fixed angular frequency ω. An important aspect of the MSEs is that they are solved for a single frequency. Thus, the source function is computed for only one frequency at a time. If the spectrum of waves is broad or bimodal, the MSEs may be solved several times, thus resulting in several source functions. The resulting single-frequency wave fields will be combined into a complete description of the wave field for final use.

Each frequency's source function is determined through an iterative process of minimizing a cost function, which is defined as:

$$J = \iint \frac{1}{2}[\eta_r(x,t) - \eta_r^{obs}(x,t)]^2 M(x,t)dxdt$$

where η_r is the radial derivative of the model estimated slope, η_r^{obs} is the observed radial slope, and $M(x,t)$ is a shadow mask. The shadow mask is a binary matrix determined using the Radar Model during computation of the radial slopes, where 1's are illuminated regions of the sea surface, and 0's are shadows between wave crests. As the model reaches a solution closer to the observed waves, the cost function is minimized.

We wish to minimize *J* subject to the constraint that the wave field is a solution of the MSEs. The resulting conditions for the minimum leads to a set of adjoint equations:

$$\alpha_{t'} = -\nabla \cdot \left(CC_g \nabla\psi\right) + (\omega^2 - k^2 CC_g)\psi$$

$$\psi_{t'} = -\alpha + M(\eta_r - \eta_r^{obs})_r$$

with

$$\frac{\partial J}{\partial S} = \psi(\mathrm{x}_s, t)$$

as the gradient of the cost function with respect to the source term. The adjoint equations are solved with the error in the present prediction of the radial slope field as input. They are solved backward in time ($t' = -t$) and serve to propagate errors in the prediction back to the time and location of corresponding errors in the source term $S(x_s, t)$. The gradient of *J* with respect to the source term, used to adjust the source term to modify *S* in a way that reduces J is computed from the solution to the adjoint equations as shown.

In each iteration, the wavemaker source *S* is updated using the gradient of the cost function, where b is a constant determined using least-squares estimation:

$$S_{\mathrm{new}} = S - b\psi(\mathrm{x}_s)$$

S is updated with S_{new} for the proceeding iterations. The forward and adjoint equations are solved iteratively until convergence of J. This procedure in the algorithm can be summarized in the following steps:

1. Assume a zero initial guess for the source function.
2. Compute the error in the radial slope (source term for the adjoint ψ equation) and execute the adjoint model.
3. Compute the gradient of the cost function with respect to the source function at the wavemaker location from the adjoint solution.
4. Adjust the source function from its initial guess using this gradient.
5. Execute the forward model for a new MSE solution; the cost function will be reduced from step 2.
6. Repeat steps 2-5 until the cost function converges.

These steps are carried out once for every specified frequency in the model configuration. The source function for each frequency is filtered to suppress contribution from other than the chosen center frequency. The size of the bandwidth used for filtering was a fixed value in the initial version of Wavecast, set to the size of the specified frequency itself. In other words, for a specified frequency of 1 Hz, the representative frequencies in the source function would range from 0.5 Hz to 1.5 Hz. The majority of the tests in this manuscript use this filtering technique. In a later version of Wavecast, the size of this bandwidth becomes a user input. Filtering using 20% of the specified frequencies is discussed in section 6. When multiple frequencies are used, the resulting wave field are combined via linear superposition to produce a complete description of the wave field.

2.4 Wave Propagation

The source function is used to initialize the waves that are propagated through the full computation domain. The source function is applied at the inner edge of the sponge layer that lies along the outer range. The waves are propagated through the domain using a finite differencing approach. The sponge layer is applied along the extreme azimuths to reduce reflection as they travel, and the inner sponge layer reduces reflection as they reach the reach the other side. The computation of the wave propagation happens in faster than real time to allow for a forecast before the actual waves arrive. The size of the domain over which the waves propagate should be chosen with consideration of the computation time and the transit time of the real waves. The larger the domain, the longer it will take the actual waves to propagate across. This lengthens the duration of minimum computation time

that must be met. However, the maximum size of the domain is limited by the size of the radar images. The assimilation domain, which is located along the outer ranges of the domain, must fall within ranges of high quality radar data. In the presented work, the size of the domain is chosen with respect to the regions of the highest quality radar data, and an optimization of grid sizing and resolution is not yet established.

2.5 Applicability of the Mild Slope Equations

Choosing a wave model for Wavecast was done by deliberately considering the application to WEC devices. A balance between accuracy and computation time must be reached to give the best possible forecast, in keeping with the capabilities of real-time estimation. Choices for phase-resolving wave models are fairly limited. The two options feasible for real-time computation are Boussinesq and Mild-Slope Equations (MSEs). Other options, such as nonlinear spectral models, potential flow models, and Navier-Stokes models are not currently feasible to solve in faster than real time. In order to choose between the Boussinesq and MSEs, the wave conditions typical of a WEC site are considered. These conditions are demonstrated in Figure 4. The abscissa is a non-dimensional parameter representing water depth, and the ordinate is a non-dimensional parameter representing wave height. Each dot represents a combination of wave height, wave period, and water depth, where height ranges from 1-8 m, period ranges from 6-16 seconds, and water depth ranges from 30-80 meters. The majority of the waves fall in the regions of linear and second order stokes waves.

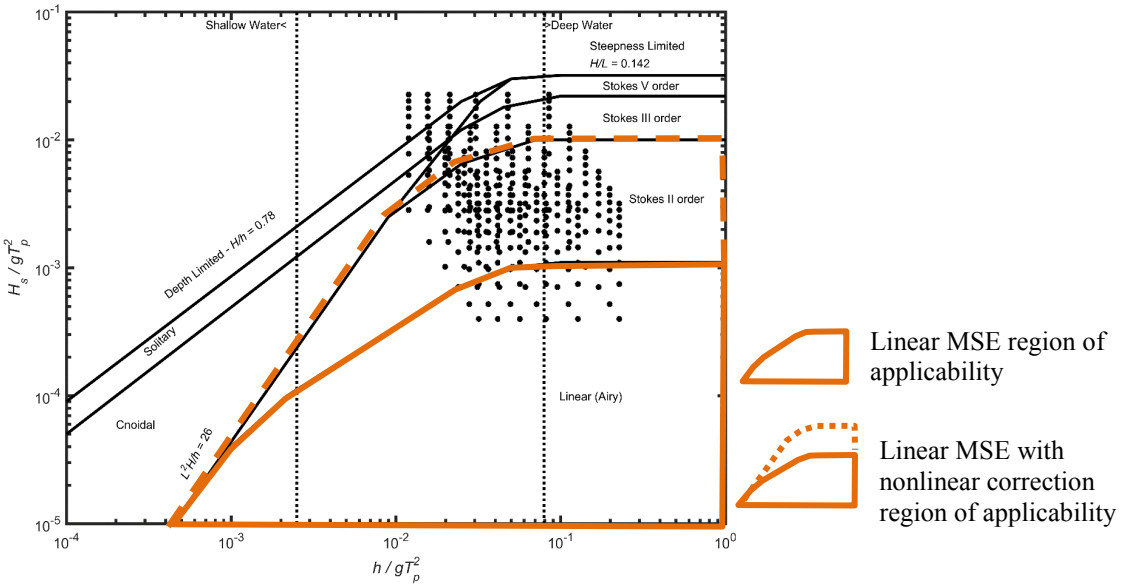

Figure 4. Wave conditions typical of a WEC site, with regions of MSE applicability.

The MSEs are used widely in intermediate to deep water depths and regions where depth-limited breaking does not need to be considered. Originally derived by Berkhoff (1972), they are linear in their typical form:

$$\frac{\partial \eta}{\partial t} + \nabla \cdot \left[\frac{CC_g}{g}\nabla\phi\right] + \frac{\left(\omega^2 - k^2 CC_g\right)}{g}\phi = 0$$

$$\frac{\partial \phi}{\partial t} + g\eta = 0$$

The current version of Wavecast is configured using the linear MSEs. However, by using nonlinear correction terms, the MSEs can account for second order stokes nonlinearities. In future versions of Wavecast, these correction term may be added.

3. The Radar Model

The radar system used for this study is a commercial X-Band marine radar operating at low grazing angles with horizontal polarization. The Radar Model is a recently derived, linear relationship between backscatter intensity *I* and the radial slope η_r of ocean waves, without the need for external calibration (Lyzenga & Walker, 2015).

For the full derivation of the Radar Model, the reader is directed to the paper by Lyzenga and Walker (2015). The base principles from which the expression is derived are the backscatter model given by perturbation theory (Valenzuela, 1978), and an expression for the backscattered power received by a radar system. Additionally, geometric shadowing is expressed analytically for consideration in the model. The expression for radial slope is derived from a series of parameter assumptions and geometric considerations. The specific assumptions made in the derivation are:

1. Radar grazing angles are small, thus incidence angle $\theta \approx \frac{\pi}{2}$ and depression angle $\theta_d \approx 0$.
2. The height of the radar is much larger than the surface elevation of the waves, $h \gg \eta$.
3. The azimuthally averaged radar signal has a fall off with range of $r^{-7/4}$.

By making these assumption, the derivation arrives at a simple and direct relationship, expressed as:

$$\eta_r(r,\phi) = \frac{h}{r}\left[\frac{I(r,\phi)}{\langle I(r,\phi)\rangle} - 1\right]$$

Using knowledge of the radar height, h, the slope of the radial component of the sea surface slope η_r can be computed at each range r, and azimuth ϕ. The value $\langle I(r,\phi)\rangle$ is the local mean of intensity at each range and azimuth location.

The first and second assumptions are properties of the radar configuration. They can both be satisfied by mounting the radar sufficiently high such that the grazing angles become small, and wave height has a negligible influence. The third assumption is based on patterns observed in various radar datasets. The intensity range dependence is considered in two radar datasets: one collected from a ship-mounted FURUNO navigation radar off the coast of Northern California, and one collected form a shore-based SITEX/Koden radar in Newport, OR. Both datasets show agreement with the assumed range dependence. This dependence is an important component in the derivation of the Radar Model. It provides validation that the averaged radar signal is independent of wave shadowing, enabling considerable simplifications to the backscatter model.

Aside from the field datasets considered in the derivation of the Radar Model, the final arrived equation has yet to be demonstrated in field use. This study serves as its first application, and thus is a first attempt at validation.

4. Synthetic Validation

Validation of the forecasting algorithm has been conducted in two phases: using synthetically-generated input conditions, and using a field dataset of radar images and in situ surface elevations. The first phase uses two datasets of synthetic radial slope values for direct assimilation in the Wavecast model. This enables testing the efficacy of the Wavecast model alone, before coupling with the Radar Model. The first synthetic dataset is a monochromatic wave field created analytically in polar coordinates. The second is a simulation of water surface elevation using a nonlinear Boussinesq model.

4.1 Monochromatic Wave Field

4.1.1 Input Conditions

A synthetic monochromatic wave field is solved for analytically in polar coordinates using an equation presented in (Naaijen & Wijaya, 2014):

$$\eta(r,\varphi,t(\varphi)) = \sum_n \sqrt{2\,S(\omega_n)d\omega}\cos\left(k_n r(\cos(\varphi),\sin(\varphi))\cdot(\cos(\theta_n),\sin(\theta_n)) - \omega_n t(\varphi) + \phi_n\right)$$

where η is the water surface elevation at each range r and azimuth φ, $\sqrt{2\,S(\omega_n)d\omega}$ is the wave amplitude, ω_n is the angular frequency, k_n is the wavenumber, θ_n is the wave propagation direction, and ϕ_n is the phase. To find the radial component of the sea surface slope, the derivative of η was taken with respect to r:

$$\eta_r\big(r,\varphi,t(\varphi)\big) = \sum_n -k_n\sqrt{2\,S(\omega_n)d\omega}\,(\cos(\varphi),\sin(\varphi))\cdot(\cos(\theta_n),\sin(\theta_n))\sin\big(k_n r(\cos(\varphi),\sin(\varphi))\cdot (\cos(\theta_n),\sin(\theta_n)) - \omega_n t(\varphi) + \phi_n\big)$$

Two synthetic datasets are generated, one for water surface elevation and one for radial slope. The amplitude is set to 1.5 m, with a period of 10 seconds and fixed water depth of 70 meters. The dataset of radial slope is used for assimilation, and the dataset of water surface elevation is used for ground truth.

4.1.2 Wavecast Domain Setup

A schematic of the computation grid is given in Figure 5. The full grid is 3000 m in range and 180 degrees in azimuth. The annulus chosen for data assimilation is 1500 m wide in range and 180 degrees in azimuth, thus incorporating half of the domain. A 1500 m wide assimilation domain is appropriate because the dominant wavelength from the simulated spectrum is 155 m. Thus, approximately 10 wavelengths can incorporated, a reasonable number for use in assimilation. The assimilation annulus is demonstrated using a blue outline. Despite only needing synthetic data within the assimilation domain for Wavecast, it is important that the simulated data exists throughout the full computation domain. This enables validation of the waves once they propagate out of the assimilation domain, thus validating forecasted waves as opposed to reconstructed waves. The sponge layer is indicated in red. It is 300 m in range and 5 degrees in azimuth. The size was chosen with some consideration of the wavelength, anticipating that the waves would be adequately absorbed given a region of two wavelengths.

Despite being a synthetic dataset, the grid is set to geographic coordinates. This is because Wavecast works in a georeferenced system, where input data is converted from UTM to East-North-Up (ENU) basis vectors. The ENU vectors allow the domain to be easily expressed in UTM, WGS-84 or Earth Centered Earth Fixed (ECEF) coordinates. For simplicity, as well as verification of these conversion techniques within the model framework, GPS coordinates were chosen for the synthetic dataset's origin. Since the synthetic dataset was created on flat-bottom bathymetry, these coordinates are somewhat arbitrary. They are in close vicinity to the field dataset collected offshore Newport, OR. The numbered points in the domain are the locations at which input and model time series will be compared in the proceeding section.

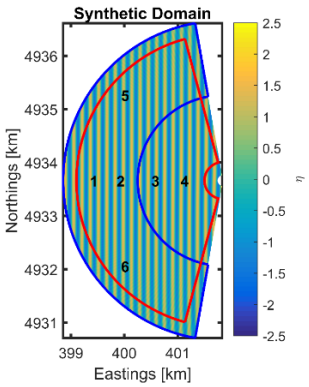

Figure 5. Schematic of Wavecast domain for monochromatic synthetic trials.

4.1.3 Monochromatic Results

Model time series from six locations throughout the computation domain are compared to the synthetically generated water surface elevation. The correlation coefficient between the two time series is computed at zero lag. First, a set of four points are looked at in the up-wave direction, shown in Figure 6. The correlation between time series within the assimilation domain (1 and 2) as well as closely after the waves leave the assimilation domain (3) is high, approximately 0.9. Closer to the origin, where the waves have traveled a further distance beyond the assimilation domain, the correlation is reduced, with a value of 0.77. There are start-up effects when the model is run, resulting in a few smaller, out of phase waves at the trailing end of the wave packet. The reason the start-up effects are at the end of the model record is because the source function is solved for in the reverse direction, so these are the first waves created in the source function solution. These start-up effects reduce the overall correlation. However, the correlation beyond these waves is good.

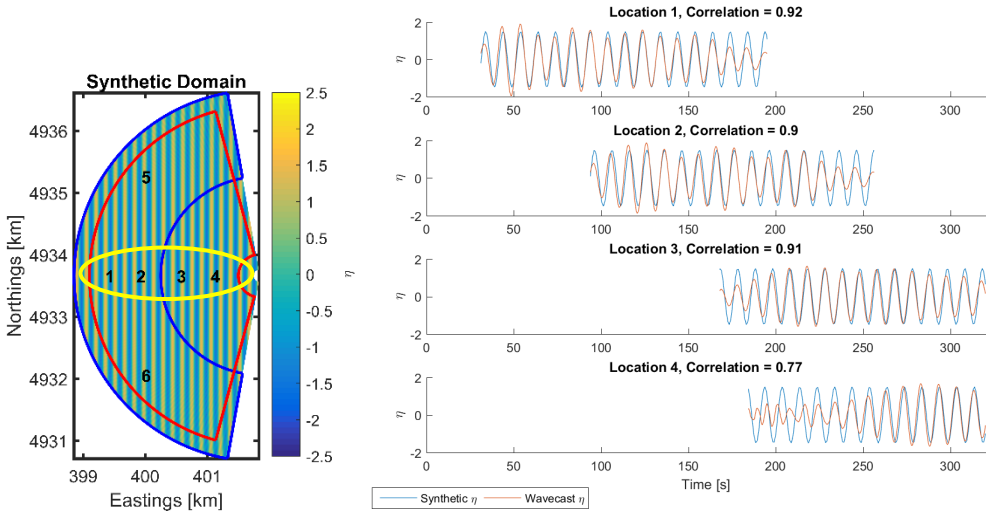

Figure 6. Monochromatic time series comparison in up-wave direction.

Two additional locations are compared in Figure 7, to show azimuthal variability. Locations 5 and 6 are at the same range as location 1, but spaced out azimuthally. The input slope data at these azimuths is no longer the pure wave slope, as the synthetic "radar" is not looking in the up-wave direction. The slope value at these locations is the radial component of the actual slope. The correlation at locations 5 and 6 is reduced from location 1. Additionally, the amplitude is reduced in the modeled surface elevation, mostly due to the fact that the input radial slope values are a reduced version of the actual slope.

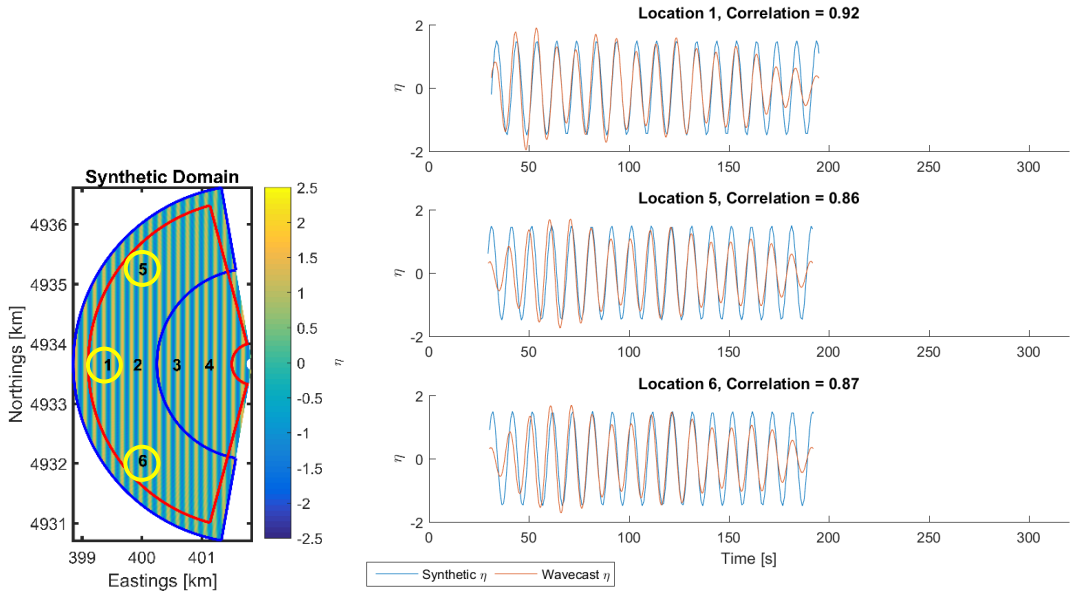

Figure 7. Monochromatic time series comparison with azimuthal variability.

The cross correlation between the modeled and input time series at every location within the domain is also considered, represented in Figure 8. The correlation throughout the domain is nearly 1. The lobes of 0 correlation at the extreme azimuths is likely due to the effect of the reduced slope, as the "radar" is looking along-crest.

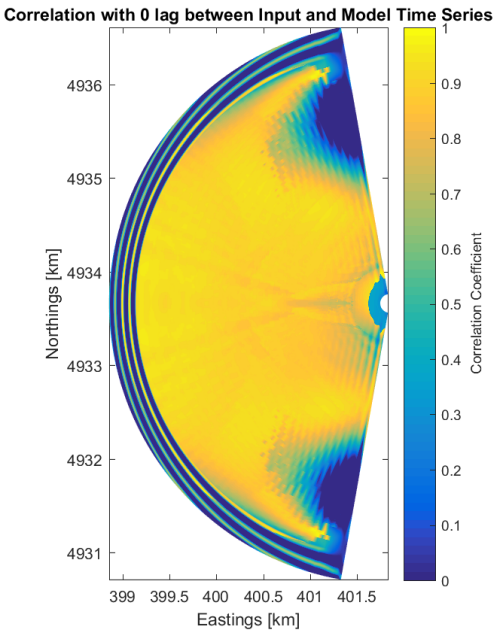

Figure 8. Correlation coefficients for the between model and synthetic water surface elevation throughout full monochromatic domain.

4.2 Nonlinear Wave Field

A nonlinear wave field is simulated using the Boussinesq wave equation. The Boussinesq equation describes the time varying surface elevation including nonlinearities and wave dispersion (Nwogu, 1993; Peregrine, 1967; Wei & Kirby, 1995). While Wavecast uses the linear MSEs, utilizing a synthetic dataset with weak nonlinearities will give a better representation of the actual sea. It will provide an understanding of how well the linear MSEs may perform in real world conditions better than a linear synthetic dataset.

4.2.1 Description of Input Conditions

A snapshot of the Boussinesq modeled surface elevation is shown in Figure 9 (a). The conditions chosen for the synthetic data are based on the spectrum from the date of field testing. There are a total of 358 frequency-direction components used. The frequency bins are truncated from 0.06 Hz (16.7 s) to 0.14 Hz (7.2 s), which eliminates a lower frequency (20 s) swell from the field data spectrum. This creates a unimodal spectrum, which enables the simplicity of solving the MSEs for a single frequency. The direction bins range from +/- 30 degrees off a chosen peak direction of 270 degrees. The bathymetry used in the Boussinesq model for the assimilated data region is flat-bottomed with depth of 70 meters.

From the surface elevation η, the component of surface slope in each radial direction, e.g. the component of slope the radar is able to detect, is computed as the spatial derivative along each range line. This is done using a simple finite differencing approach, where for each range r and azimuth φ, the radial slope η_r is:

$$\eta_r(r_i, \phi_i) = \frac{\eta(r_{i+1}, \phi) - \eta(r_{i-1}, \phi)}{2\,\Delta r}$$

The radial slope is shown in Figure 9 (b). This becomes the input to the Wavecast system. By utilizing a synthetic dataset of radial slope, the use of the Radar Model has been bypassed, allowing for validation of the Wavecast algorithm alone.

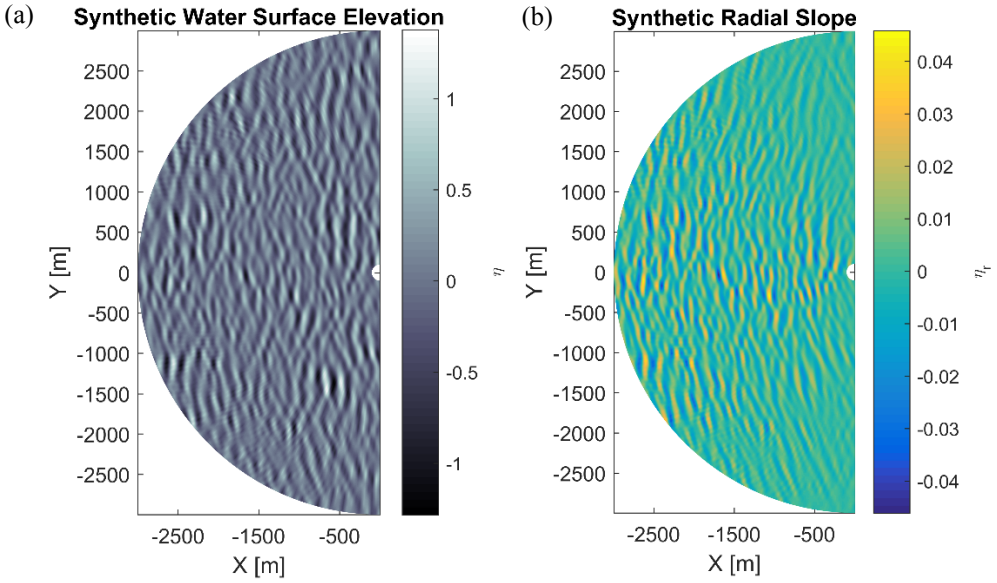

Figure 9. Synthetic dataset for Wavecast validation: (a) Synthetic water surface elevation computed using nonlinear Boussinesq model, and (b) Synthetic radial slope from finite differencing of (a).

4.2.2. Wavecast Domain Setup

The same model domain configuration is used for the nonlinear surface elevation trials as in the monochromatic cases. This domain is described in section 4.1.2, and is shown again in

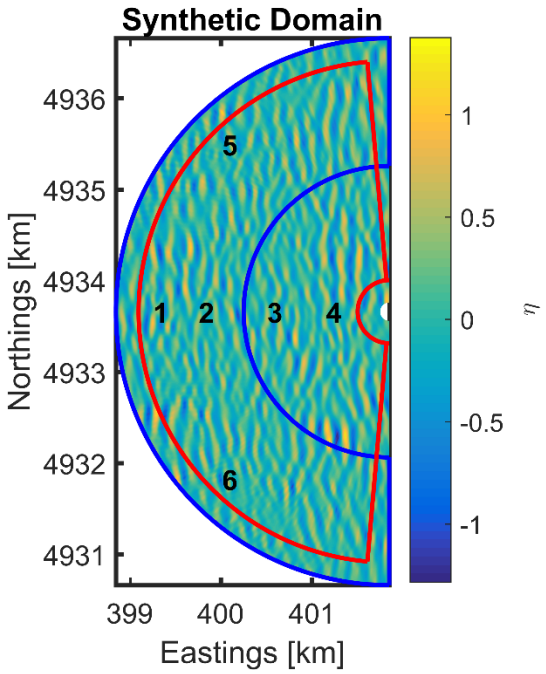

Figure 10. Schematic of Wavecast domain for nonlinear synthetic trials.

4.2.3 Results from Wavecast

While a considerable number of trials have been executed to understand the optimal configuration settings in Wavecast, model results from two sets of characteristic synthetic cases are presented here. The first set of testing looks at the effects of the chosen frequencies on the Wavecast results. The second set of testing looks at the duration of data assimilation. The parameters used for assessing model performance are listed and described in Table 1.

Table 1. Description of Model Parameters

Parameter	Description
Model Cost	The value reached by the cost function at convergence, where 0 means the model waves and observed waves are identical, and 1 means no correlation.
Assimilation/Prediction (s)	Both model time specifications are listed here. The assimilation time is the duration of data used for assimilation. The prediction time is the length the simulation is carried out after the wavemaker source function has been used.
Num. Freqs.	The number of frequencies specified for solution to the MSEs. One source function is solved for each frequency.
Freqs. (rad/s)	The frequency values specified.
Filtering Bandwidths (rad/s) *	The bandwidth of the filtering applied to the source functions of the corresponding frequencies. If no bandwidth is specified, it is the size of the frequency specified.
Period (s)	2π/Freqs

% H reconstructed	The percent of the significant wave height reconstructed in the model spectrum. $\frac{4\sqrt{m_{0-model}}}{4\sqrt{m_{0-target}}} x100$
Correlation at 0 lag **	The correlation coefficient associated with the zero-lagged model and target time series.

* for filtered Synthetic and Field trials only
** for Synthetic trials only

4.2.4 Frequency Trials

The frequencies specified in the Wavecast configuration are the frequencies at which the MSEs are solved to arrive at the wavemaker source function. Thus, the number of frequencies chosen and their values is an important component of accurately reconstructing the waves within the domain. Specifically, the chosen frequencies determine the phase speed of the waves in the source function. All of the waves in a given source function will propagate at the speed of that source function's chosen frequency. In the initial version of Wavecast, each of the source functions for each specified frequency is filtered using the size of that frequency. Four synthetic cases with varying specified frequencies are summarized in Table 2.

Table 2. Summary of Synthetic Trials: Frequency Testing

Run Name	Model Cost	Assimilation/ Prediction Times (s)	Num. Freqs.	Freqs. (rad/s)	Period (s)	% H reconstructed at 2	Correlation at 0 lag					
							Loc. 1	Loc.2	Loc.3	Loc.4	Loc. 5	Loc. 6
Synthetic1	0.6466	400/400	1	0.628	10	83.08	0.86	0.9	0.67	0.29	0.83	0.82
Synthetic2	0.7222	400/400	2	0.56549, 0.83503	11.1, 7.5	80.03	0.87	0.72	0.51	0.39	0.76	0.82
Synthetic3	0.6474	400/400	3	0.56549, 0.70026 0.83503	11.1, 9.0, 7.5	79.09	0.9	0.94	0.36	0.07	0.83	0.92

In Synthetic1, a single frequency was chosen of 0.1 Hz. Thus, the filtering on the source function will range from 0.5 Hz to 1.5 Hz. Considering the frequencies used for creating the synthetic dataset range from 0.6 Hz to 1.4 Hz, using a frequency at the midpoint is a logical choice. A map of significant wave height is shown in Figure 11 (a). A spectrum is shown in Figure 11 (b), which was created from the time series at the location of the diamond in Figure 11 (a). The significant wave height computed from the spectrum is 1.06 m, which is 83 % of the anticipated Hsig from the input conditions at the same location. The wave heights are reconstructed similarly throughout the center azimuths of the domain. At the outermost azimuths, approx. +/- 20 degrees from the edges of the domain, the wave heights tend to decay. This is because of the azimuthal decay of the radial slope input conditions. While Wavecast is expected to consider that the slopes given are the radial component, the slope information is incomplete.

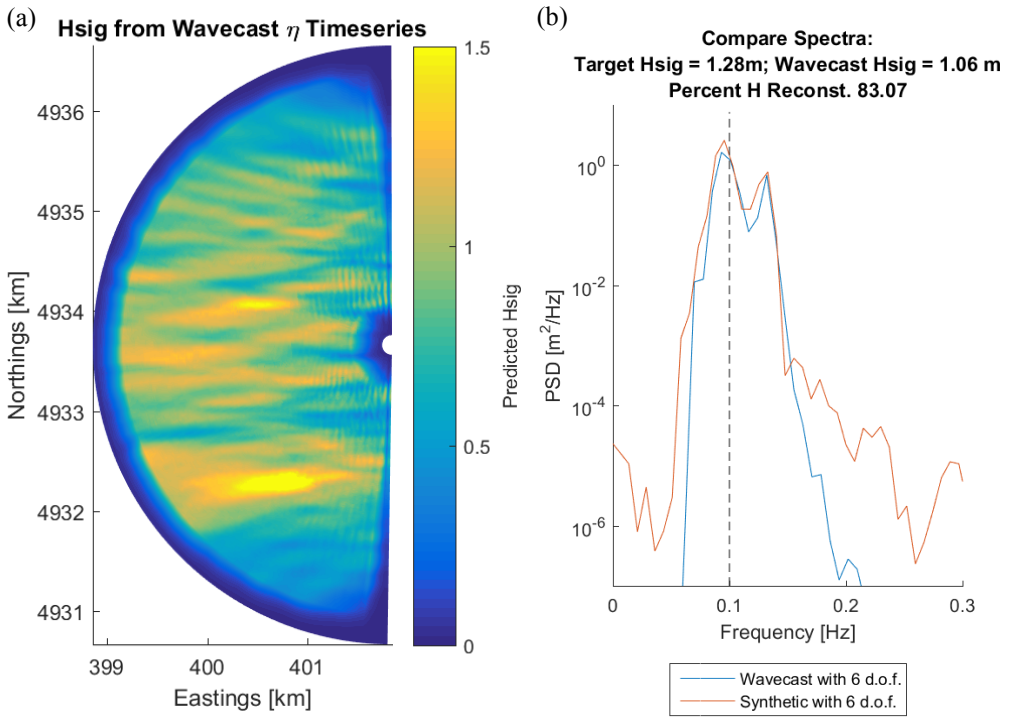

Figure 11. Results from Trial Synthetic1: (a) Map of significant wave height of model waves throughout domain and (b) Comparison of input to output spectra computed at Location 2.

This chosen frequency reconstructs the wave heights at location 1 up to 83%. Next, the individual time series from Syntehtic1 will be considered. Time series from the six locations indicated in the domain schematic (Figure 10) are shown in Figure 12 (up-wave) and Figure 13 (azimuthally variable).

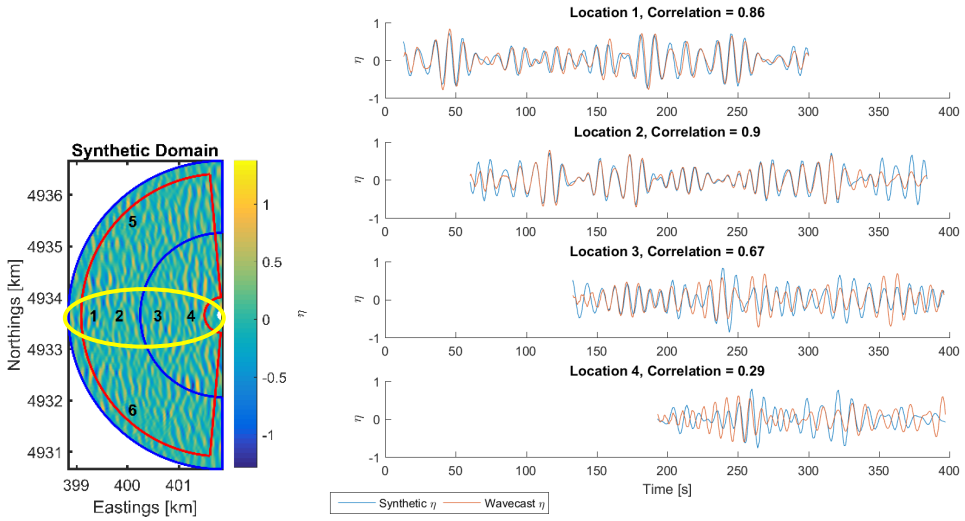

Figure 12. Nonlinear time series comparison in up-wave direction.

The correlation is the highest at locations 1 and 2. These two locations are within the assimilation domain, and are therefore reconstructed waves as opposed to predicted waves. It makes sense that these waves would be well reconstructed because the source function is generated based on knowledge of these waves in order to best reproduce these waves. As the waves leave the assimilation domain, the correlation decreases. This indicates that there is an error in the propagation of the waves. At present, it is not possible to determine whether this error is due to model accuracy or due to a mismatch in wave physics between input and model wave equations. If the error were due to the former, it would be because all of the frequencies present in the source function are being propagated at single phase and group speeds, the speed associated with the specified frequency. If the error were due to the latter, it would be because the model is solving the mild slope equation, a linear wave equation, while the input data was generated using the nonlinear Boussinesq equation.

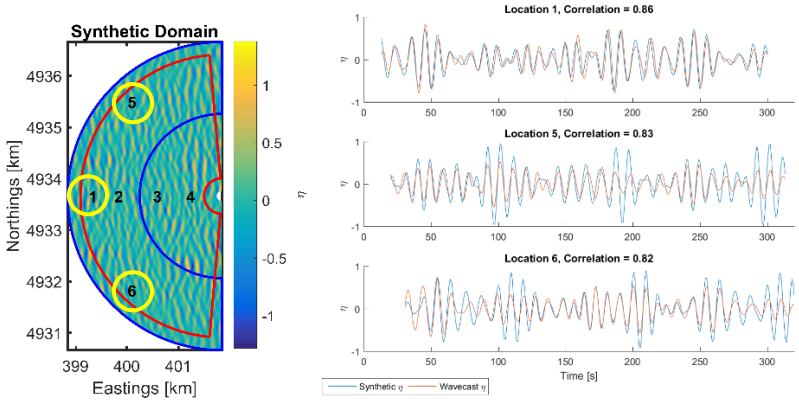

Figure 13. Nonlinear time series comparison with azimuthal variability.

Figure 13 shows time series correlation at locations with azimuthal variability, +/- 45 degrees from location 1. At locations 5 and 6, the correlation is reduced from location 1. The phase correlation appears to be good, however there is a reduction in the wave amplitude. This is likely because the input data is the radial component of surface slope, a reduced value from the actual surface slope.

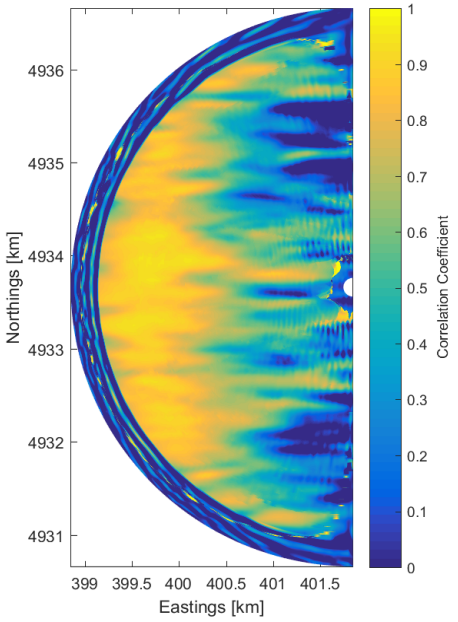

Figure 14. Correlation coefficients at 0 lag from Synthetic1.

Figure 14 shows the cross-correlation between input and model data at every point throughout the model domain. The correlation is high throughout the assimilation region, however it decreases as the waves propagate out of the assimilation region and into the prediction region.

Trials 2 and 4 use two frequencies as opposed to one, but with worsened results than Trial 1. Trial 3 uses a single frequency, chosen because it is the peak of the input spectrum, also with worsened results. It is hypothesized that these results are due to the fact that the size of the bandwidth filtering on the frequency causes frequencies outside of the input spectrum to be included. These will not be modeled accurately by the MSEs as they are nonlinear components of the Boussinesq model. Trial 1 likely yields the best results because its bandwidth lies within the frequency bounds of the input spectrum.

4.2.5 Duration of Assimilation Trials

Optimizing the accuracy of the prediction with the duration of assimilation is important for real-time forecasting. Collecting data for assimilation contributes to the total time it takes to forecast the waves. Synthetic1, the best case run from the frequency trials is repeated using varying assimilation lengths. In Synthetic5, a 200 second assimilation is used, and the accuracy of the forecasted waves is compromised. Interestingly, the correlation between the time series at Location 4 is quite good. It is unclear at this time whether this is a positive artifact or a coincidence that the phases aligned. In Synthetic6, a 100 second assimilation is used, and virtually no waves are reconstructed by

Wavecast. We conclude that 400 seconds is an appropriate assimilation duration for reconstruction of the synthetic waves using the presented domain configuration and frequency filtering.

Table 3. Summary of Synthetic Trials: Assimilation Duration Testing

Run Name	Model Cost	Assimilation/ Prediction Times (s)	Num. Freqs.	Freqs. (rad/s)	Period (s)	% H reconstructed at 2	Correlation at 0 lag			
							Loc. 1	Loc.2	Loc.3	Loc.4
Synthetic1	0.6466	400/400	1	0.628	10	83.08	0.6	0.73	0.63	-0.04
Synthetic5	0.8482	200/200	1	0.628	10	45.69	0.36	0.36	0.31	0.33
Synthetic6	0.9998	100/100	1	0.628	10	0.47	0.06	0.04	-0.03	0.09

5. Shipboard Field Validation

To validate the coupled Wavecast system with the incorporation of the Radar Model, a field dataset was collected. This dataset is comprised of radar observations, as well as a time series of in situ surface elevation data recorded at a location inside the radar domain. These temporally and spatially overlapping data allow a phase-resolved comparison between the system's forecasted waves and the actual waves at the point location of the buoy.

5.1 Field Data Collection

5.1.1 Radar Data

On December 15, 2015, the dataset of radar and in situ surface elevation measurements was collected offshore Newport, OR. The radar was mounted onboard the Umatilla II, a 50 ft. charter fishing vessel that can be seen in Figure 15 (a). In situ surface elevation data was recorded by a TRIAXYS Directional Wave Buoy, owned and operated by the Northwest National Marine Renewable Energy Center. The TRIAXYS buoy can be seen from onboard the Umatilla II in Figure 15 (b).

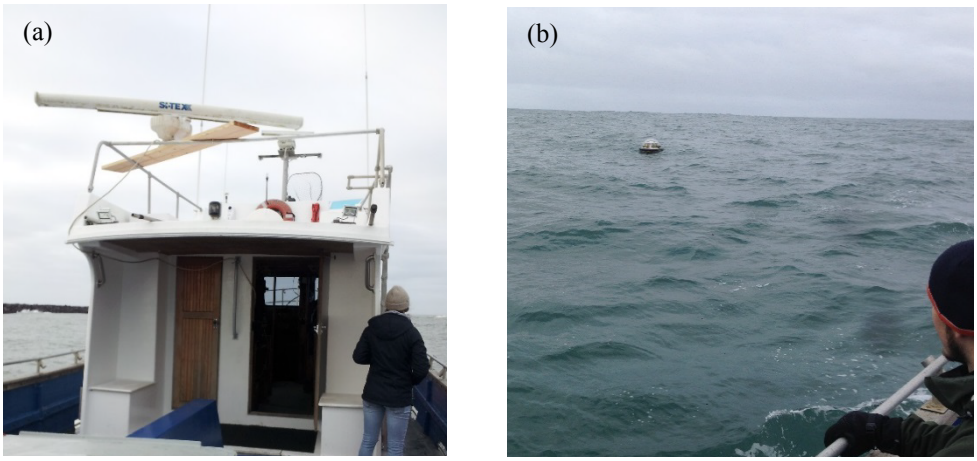

Figure 15. (a) Oregon State University's X-Band Marine Radar mounted onboard the charter fishing vessel Umatilla II, and (b) the TRIAXYS Directional Wave Buoy visible from the Umatilla II.

Although field testing was anticipated for early November, it was delayed due to persistent storms on the Oregon coast. The operable conditions for the Umatilla II were wave heights less than 4 m. December 15 was chosen as it was the first day during a several week period with wave heights meeting this requirement.

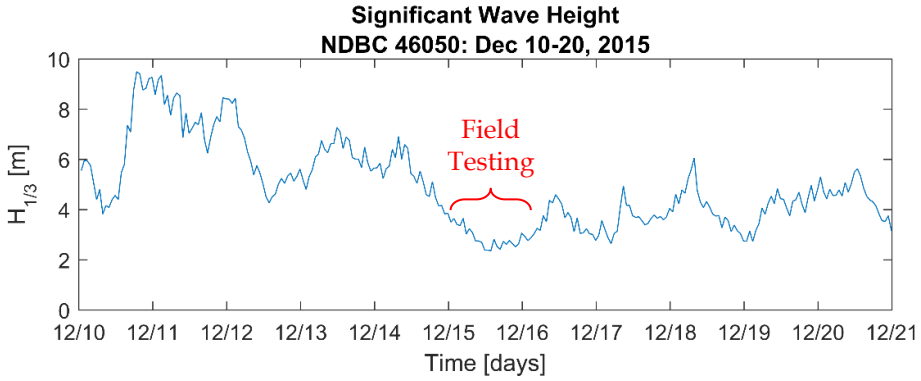

Figure 16. Significant wave height in December, 2015. Data collection was performed on December 15 during an operable window for the Umatilla II.

The meteorological conditions on December 15 were fairly complex. The frequency spectrum and directional spectrum collected by the TRIAXYS buoy during the field data collection period are shown in Figure 17 (a) and (b), respectively. The spectrum is bimodal; both a 11s swell and 20s swell were present. These are particularly challenging conditions for the Wavecast system because of the fact that the MSE is solved for a single frequency at a time. Thus, in order to reconstruct both swells, a

minimum of two frequencies will need to be specified, enabling one solution to the MSEs for each peak.

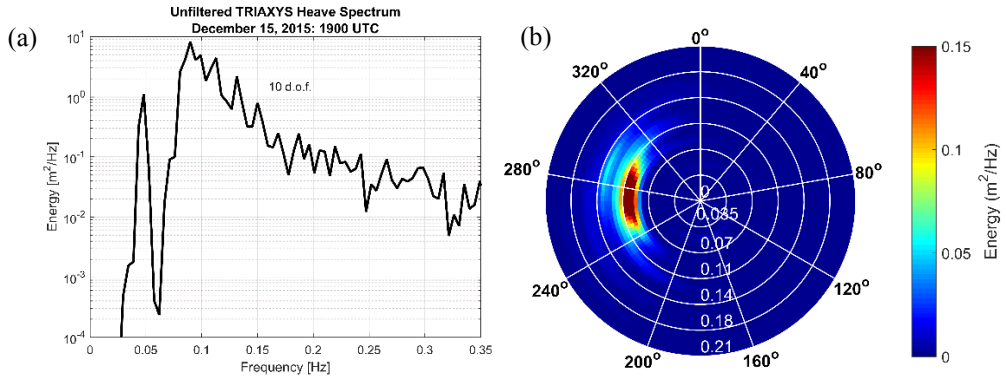

Figure 17. Spectra from the TRIAXYS Wave Profiling Buoy: (a) Frequency spectrum and (b) Directional spectrum.

An additional challenge during data collection was that the relative wind and wave directions were non-ideal for radar data collection. Optimal images are collected when the radar is looking in the same direction as the wind. Reports from the National Data Buoy Center (NDBC) Station 46050 are shown in Table 4. Throughout the data collection period, the wind direction shifted from perpendicular to the waves, to the same direction as the waves. In the field dataset, the radar captures the up-wave data while also looking upwind. Although the wave data while looking down-wave is richer because the radar is looking downwind, down-wave data cannot be assimilated in Wavecast.

Table 4. Meteorological conditions reported by NDBC Station 46050 during field data collection.

Time	Wind Direction	Wind Speed	Wave Height	Dominant Period	Wave Direction
1850 UTC 12-15-2015	180 °T	5.8 m/s	2.73 m	10.81 s	273 °T
1950 UTC 12-15-2015	255 °T	4.9 m/s	2.61 m	11.43 s	291 °T

The Umatilla II GPS track can be seen in red in Figure 18. The TRIAXYS buoy was sighted at approx.1800 UTC, then the vessel was positioned several hundred meters away. This is because data in the inner 100-200 m ring of a radar scan is not usable as the grazing angle at these ranges is too large. Once an optimal distance from the buoy was reached, the vessel was allowed to drift for approximately 1.25 hours. This stretch of the GPS track can be identified as the vertical line underneath the Umatilla II in Figure 18.

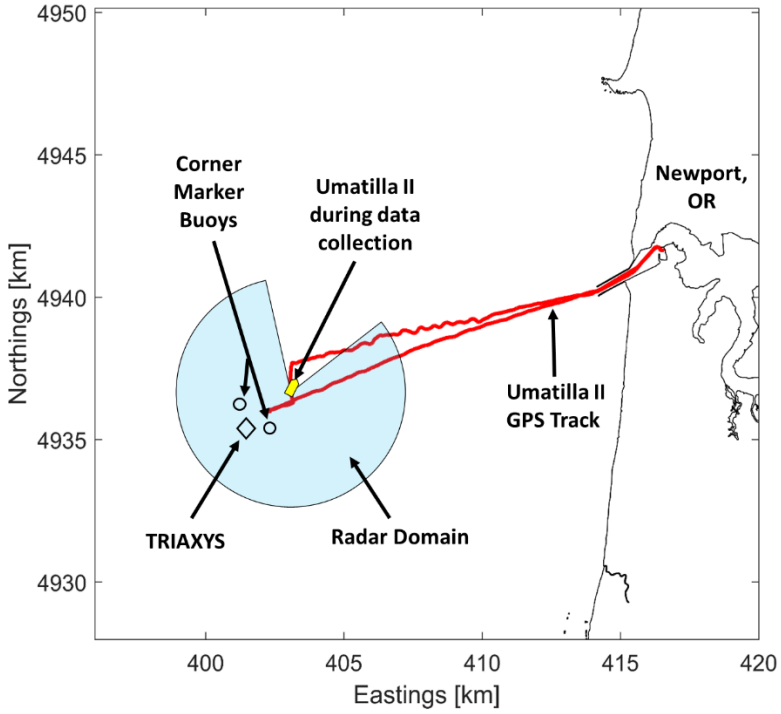

Figure 18. Schematic of field data collection conducted on December 15, 2015.

In addition to geographic coordinates, the GPS's built-in electronic compass recorded the vessel's heading, shown in Figure 19. The intention of this data collection was to account for the vessel's rotational motion throughout the drifting period. However, as will be discussed in section 5.2, the heading data ended up being too noisy to be useful in correcting for the ship's rotational motion.

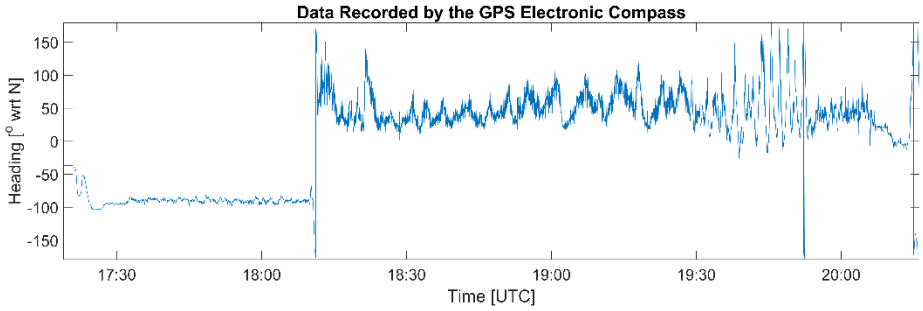

Figure 19. Heading data recorded by the GPS Electronic Compass.

5.1.2 TRIAXYS Wave Profiling Buoy

The TRIAXYS buoy was retrieved in early January of 2016. It records surface elevation data with 0.78 s sampling for 20 minutes starting at the top of every hour. Thus, throughout the drifting period, there was a 20 minute window of temporally overlapping radar and surface elevation data (1900 –

1920 UTC). This 20 minute overlapping data window becomes the field dataset used for the validation attempts in the proceeding sections.

The raw TRIAXYS heave data is shown in Figure 20 (a). The heave data is filtered to a frequency range of radar detectability. The shortest period that can be resolved by the radar is determined using the spatial range resolution of the radar. The minimum along-range discrimination of the radar is 12 m. This is the shortest wavelength, L, that the radar can resolve. The water depth, h, at the TRIAXYS location is 64 m. Thus, using the linear dispersion relationship, this translates to a wave period of 2.8 s, or a frequency of 0.36 Hz. Given the sampling rate of the TRIAXYS (0.78 s), the closest filter size to remove all frequencies higher 0.36 Hz is a 0.32 Hz filter. The TRIAXYS heave filtered at 0.32 Hz is shown in Figure 20 (b). Filtering the TRIAXYS heave data reduces the significant wave height from 2.4 m to 1.7 m.

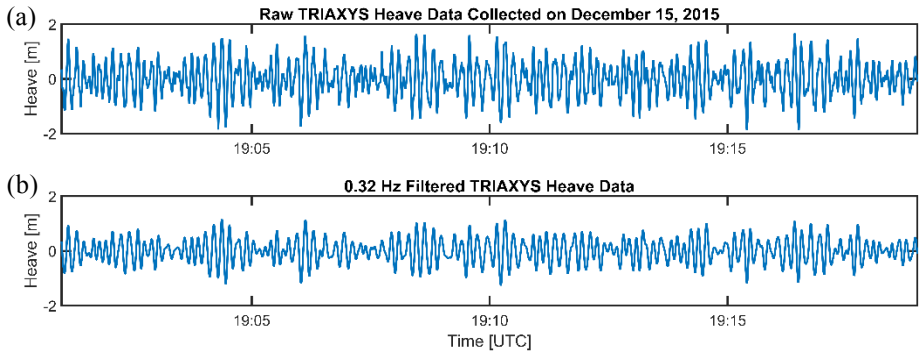

Figure 20. (a) Raw heave data recorded by the TRIAXYS Directional Wave Buoy during field testing, (b) Heave filtered at 0.32 Hz for compatibility with radar resolution.

5.2 Field Data Processing

Mounting the radar on a moving platform introduces uncertainty to the location and heading of each radar scan. Rectifying the radar's location and orientation is necessary for utilizing the radar images in the forecasting algorithm. Additionally, the coordinates of the radar images must be known to identify the time location of the TRIAXYS buoy within the domain. There are two major sources of motion introduced by the ship that need to be corrected: drift due to current and tides, and heading rotations due to vessel motions as it rolls over the waves. The vertical heave of the vessel was not accounted for in this study. This is because a vertical displacement of the radar on the order of meters is negligible at the far (>600 m) ranges of data uses in the study.

The anticipated method of correcting for these ship motions was to utilize the recorded GPS data during post-processing of the radar images. The coordinates recorded by the GPS are satisfactory for georeferencing the ship's geographic location. However, the heading data recorded by the electronic

compass shown in Figure 19 is too noisy to accurately rectify the orientation of each radar scan azimuthally. Instead, a two-phase cross-correlation scheme was developed that uses the wave features within the scans themselves to stabilize the scan-to-scan rotations without needing the recorded heading data. In phase one, a set of "effective headings" are determined that account for scan-to-scan rotations. In phase two, the set of stable scans are azimuthally oriented to the GPS locations of two corner marker buoys, visible in 10-frame running averages.

5.2.1 Post-Processing Scheme: Phase 1

In the first phase of the correlation scheme, the waves are treated as stationary features in the domain. In other words, it is assumed that the waves in each successive scan should be in close to the same orientation. The cross-correlation between consecutive pairs of scans is found. The rotation that causes the waves in one scan to line up with maximum correlation to the waves in the previous scan is treated as the "correction rotation" between those two scans. A time series of correction rotations is recorded between each pair of scans, shown in Figure 21.

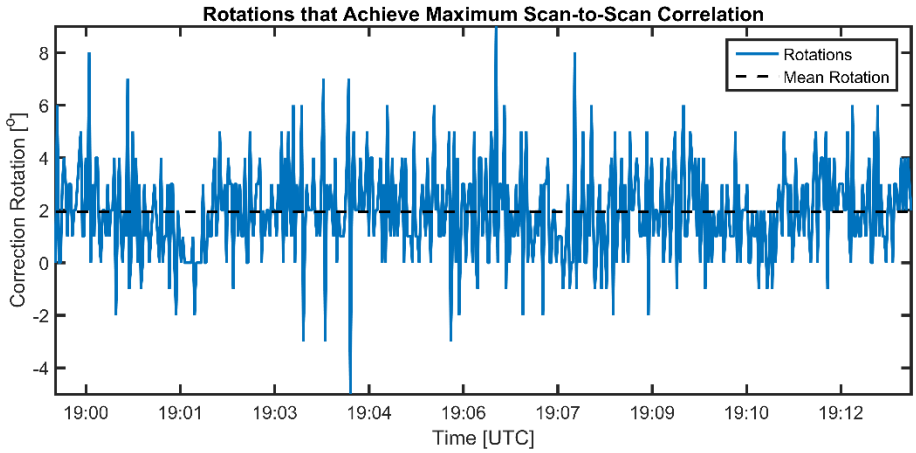

Figure 21. Scan-to-scan angular rotations determined from first phase of two-phase cross correlation scheme.

When the time series of rotations shown in Figure 21 is applied to the raw radar scans, there is a constant rotation throughout the radar time series. This is because of the assumption that the waves are stationary features scan-to-scan. In actuality, the waves are travelling forward through the radar domain. To account for this forward motion, the mean of the correction rotations over time is subtracted. When this mean is removed, the resulting time series is a set of rotations that effectively stabilize the radar rotations. This time series is shown in Figure 22. These values can be considered the "effective headings" that properly account for the ship's rotation at sea. It can be seen that this time series is considerably less noisy than the actual recorded headings shown in Figure 19.

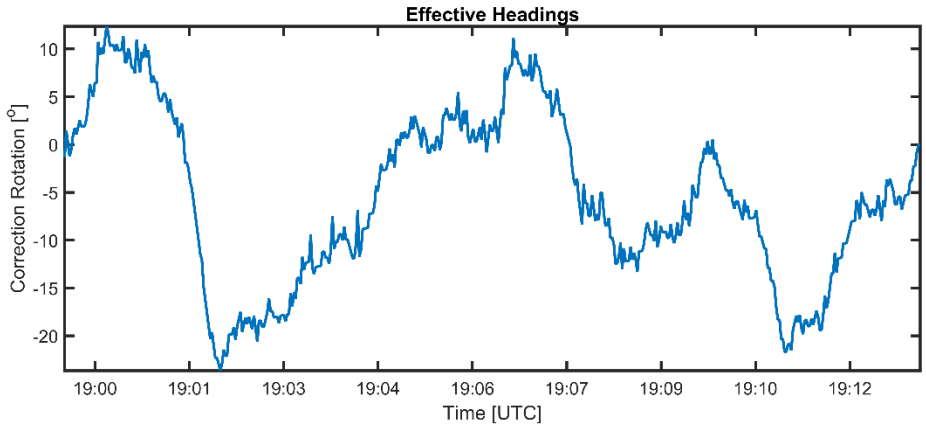

Figure 22. "Effective Headings" found from 2D cross correlation between consecutive raw radar scans.

5.2.2 Post-Processing Scheme: Phase 2

The effective headings account for the scan-to-scan rotations present in the radar data. However, there is one key component that the effective headings cannot account for: the geographic azimuthal orientation of the radar scans. The effective headings provide rotations that are only valuable as a relationship between scans, but not to geographic space. Thus, a secondary phase in the correction phase is required. It should be noted that the GPS coordinates do provide geographic knowledge of the origin of each radar scan but do not directly enable orientation of the scans azimuthally.

Once the radar scans are approximately fixed in their azimuthal orientation with respect to the wave field, it became possible to make 10-scan running averaged images in which the corner marker buoys are made visible. These key features are indicated in the field data schematic shown in Figure 18. It is not possible to confidently identify their locations in the presence of wave features. Taking a running average of the corrected scans removes the wave features, while the stationary buoys become visible. The corner marker buoys are then treated as fixed, known geographic locations. It should be noted that the TRIAXYS buoy is not a visible feature in the scans, likely because of its smaller size and less reflective material than the corner marker buoys. The running average of the first 10 raw radar images is shown in Figure 23 (a), in which the corner marker buoys are not visible. They become visible in the running average of the corrected radar scans, shown in Figure 23 (b) and zoomed in Figure 23 (c).

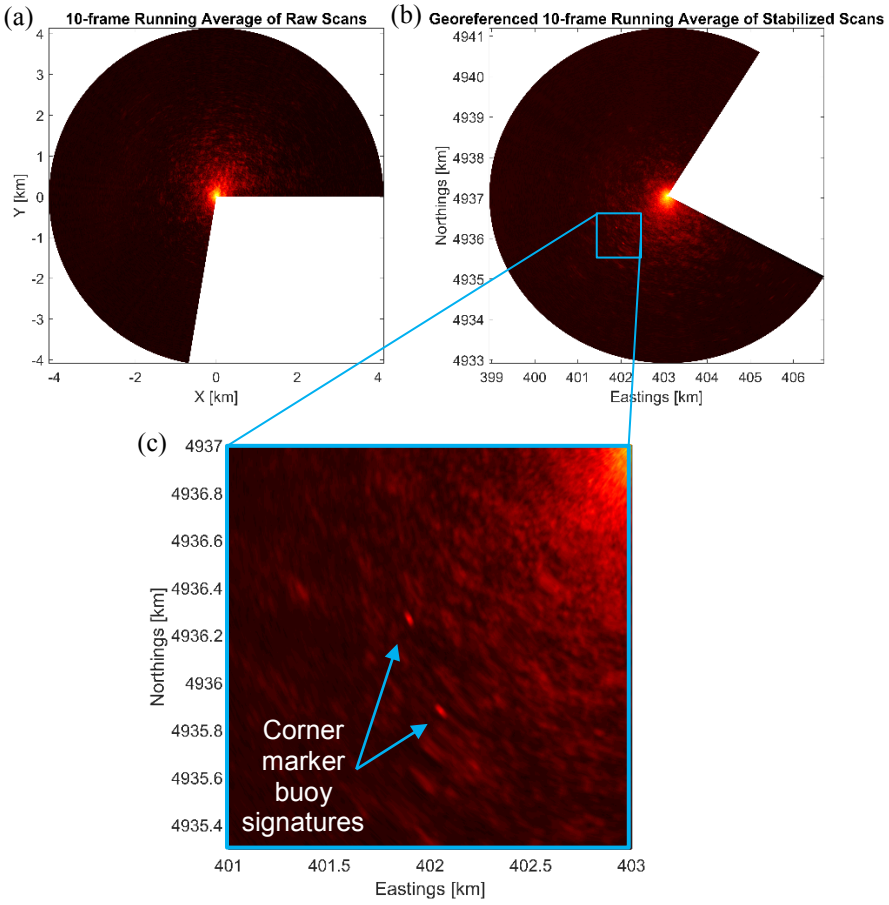

Figure 23. Corrected radar scans after first phase of two-phase cross correlation scheme: (a) shows the a 10-frame running average of the raw data, (b) shows a 10-frame running average of the stabilized data, in which signatures of the corner marker buoys are visible. (c) shows a zoom in on the corner marker buoys from plot (b).

The corner marker buoys provide the ability to locate the scans geographically in the two-phase cross correlation scheme. The locations of the two corner marker buoys are recorded several times per day, and the minimum sensitivity of their tracking software is 50 m in any direction. The best available position information for use during our data collection window is: at 1811 UTC the East buoy recorded coordinates of 402247.4 E, 4935827.3 N and at 1703 UTC the North buoy recorded coordinates of 402032.8 E, 4936168.3 N. There is of course some uncertainty in these values given the course temporal and spatial resolution of the measurements. Despite, the buoys can be used for referencing the radar scans in space, aka georeferencing.

An artificial radar scan is created for referencing against. This radar scan is the same size as the raw radar scans, however all it contains is a delta function at each corner marker buoy location.

Each 10-frame running average scan that resulted from phase one is cross correlated to this reference scan. Thus, a rotation value can be determined that best aligns the corner marker buoy signatures to the known corner marker buoy locations. This provides to benefits. Most importantly, the radar scans are oriented geographically in space. When the origin of the grid is set to the known GPS coordinate at each scan's collection time, a Northing and Easting grid can be generated. The secondary benefit is that cross referencing to the fixed corner marker buoy positions provides additional stabilization of the scans. The corner marker buoys are more fixed in space than the wave features correlated against in phase one. After this second phase of cross correlation, the time series of radar scans is noticeably less wiggly than after the first phase of cross correlation.

5.2.3 Computation of Radial Slope

Following the two-phase cross correlation scheme, the radar dataset is now (1) corrected for ship rotation and (2) located geographically. A Northing and Easting grid exists for every radar scan in the dataset. The Radar Model can now be applied to this dataset to convert the intensity values to radial slopes. A scan of georeferenced radial slope data is shown in Figure 24 (a).

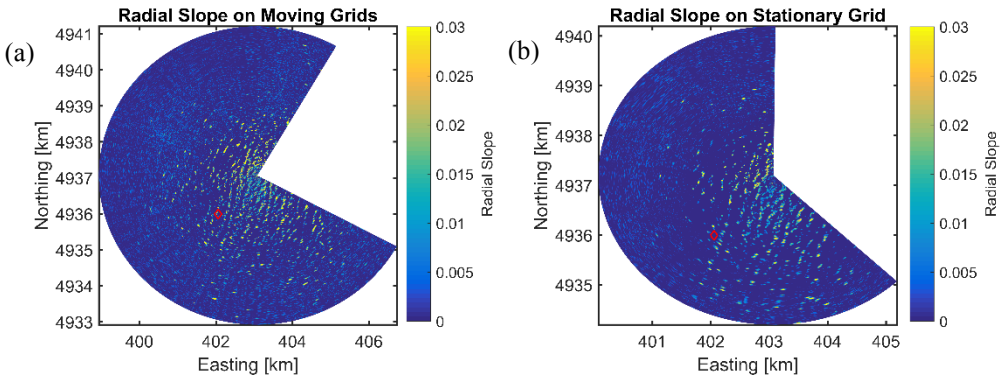

Figure 24. A single scan of radial slopes computed from the georeferenced Umatilla II intensity data (a) before interpolation onto stationary grid and (b) after interpolation onto stationary grid.

The radial slope dataset cannot yet be assimilated in Wavecast. Despite being accurately georeferenced, the dataset is still moving through space due to the ship's drifting motion. A requirement of Wavecast is that data be plotted on a single stationary grid. The midpoint of this timeframe's GPS track is chosen as the origin of a new domain. Because the radar is, in essence, travelling through this domain over time, the new grid must be smaller than the original grid so that only the data overlapping with the stationary grid is retained. The stationary grid size is chosen such that through the entire time window, there are no regions left without data. The stationary grid is

shown in Figure 24 (b). Now that the entire radial slope dataset can be plotted on a single stationary grid, the offshore field data is ready for assimilation in Wavecast.

5.2.4 Quantification of Location Errors

Phase-resolved validation of Wavecast requires time series comparison of the TRIAXYS heave data, and the TRIAXYS location within the model domain. However, two sources of uncertainty affect the location of the TRIAXYS in the model domain. These are discussed and roughly quantified.

The first source of uncertainty is the movement of the TRIAXYS itself. Its location will be treated as stationary throughout the duration of model run so that the TRIAXYS heave can be compared to the time series in a single grid cell of the model domain. However, in reality, the TRIAXYS drifts with waves, tides and currents. This drifting motion can be quantified to provide a range of uncertainty. In addition to providing heave data, the TRIAXYS records North and East motions with 0.78 s sampling, and GPS coordinates on the top of every hour. The East and North motions provide information of the buoy's motion due to waves. Throughout the data collection time period of 1900-1920 UTC, the standard deviations of the East and North motions are 0.70 and 0.48 m respectively. Since the model grid resolution is 3-4 square meters in the region of the TRIAXYS, these wave induced motions will not have an effect in choosing the model domain coordinates representative of the TRIAXYS. However, the GPS coordinates do indicate that there is drift on longer time scales, due to tides and currents. Between the hourly recordings at 1800 and 1900 UTC, the net drift distance is 10.8 m. Between 1900 and 2000 UTC, the buoy drifted 5.0 m. An uncertainty of approximately 15 meters is anticipated due to TRIAXYS movement.

The second source of uncertainty is the drift of the corner marker buoys. Since the corner marker buoys are used to georeferenced the radar scans, any error in their geographic coordinates is directly translated to the grid. Only two GPS recordings are available from the date of our data collection. There exists a coordinate for the East corner marker buoy at 1700 UTC, and the North corner marker buoy at 1600 UTC. The sensitivity of the tracking software is 50 m. Therefore, 50 m of uncertainty in the corner marker buoy locations is added to our total location uncertainty.

The total uncertainty expected in the location of the TRIAXYS is the sum of the TRIAXYS drift and sensitivity of the corner marker buoy measurements. Thus, it is expected that the model time series most closely matching the TRIAXYS time series is within a 65 m range of the 1900 UTC TRIAXYS coordinates.

5.3 Assimilation of Field Data

This section discusses the procedure for choosing the region of data for assimilation within the stationary radial slope data, as well as the size and orientation of the computation domain for inclusion of the TRIAXYS buoy.

5.3.1 Choosing the best data

The field dataset does not contain useful information at all azimuths and ranges. This is because the radar intensity of backscatter return falls off with range, and the amount of shadowing between wave crests increases. Additionally, there is no useful slope information when the radar is looking along a wave crest. Thus, a region of good wave data in the up-wave direction needs to be strategically identified. To do this, it is possible to quantify how many wave features are present along a range line at a given azimuth. The first step in this analysis is to determine what constitutes a wave feature. A threshold for radial slope is determined, for which a value falling below this threshold is not a wave and a value exceeding this threshold may be considered a wave feature.

The threshold of wave features can be estimated by computing a ballpark radial slope value from the filtered TRIAXYS heave data, shown in Figure 20 (b). From the filtered heave, the time derivative of the water surface elevation is computed, η_t. The time derivative is related to the spatial derivative of the water surface elevation through the relationship:

$$\eta_x = \frac{\eta_t}{C}$$

The celerity, C, is computed using the peak frequency of the TRIAXYS spectrum. The η_t time series is divided by the mean wave celerity, resulting in a spatial derivative of the water surface elevation, η_x. The RMS value of η_x for the TRIAXYS heave time series is 0.02. This value becomes the threshold value; all slope values that exceeds this 0.02 threshold are considered wave features.

The azimuth in the up-wave direction is chosen for the range transect. This is because the threshold value of 0.02 represents the absolute slope of the waves, where x is in the direction of wave travel. When the radar is looking directly into the faces of the waves, the radial component of the surface slope will be, most nearly, the same value as η_x. The up-wave range transect is indicated in Figure 25 (a). This range transect is plotted over time in Figure 25 (b). A binary mask is applied, where all values below the 0.02 slope threshold are assigned a value of 0, and all values equal to or exceeding the 0.02 slope threshold are assigned a value of 1. Thus, only definitive wave features are retained. The highest density of linear features shows up in ranges of 400 to 1500 meters. Data within these ranges are chosen for assimilation in Wavecast.

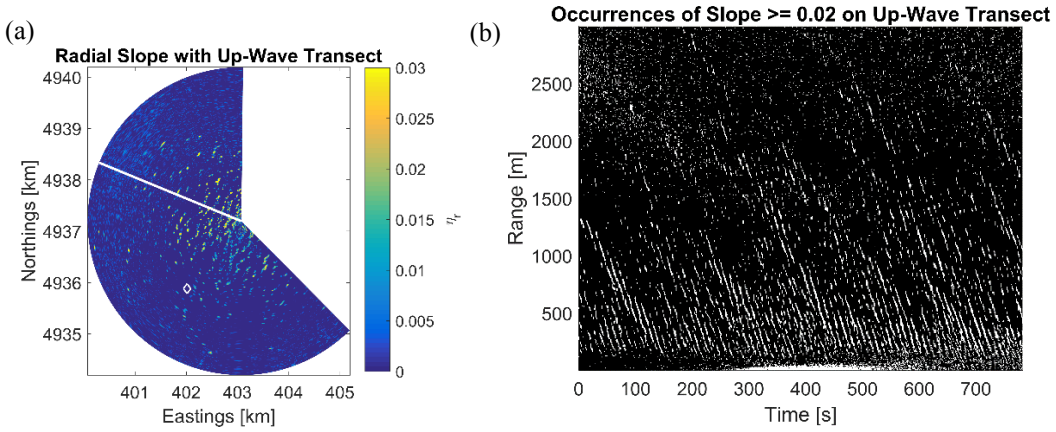

Figure 25. Choosing regions of assimilation data: (a) radial slope showing transect in up-wave direction and location of TRIAXYS, (b) occurrences of radial slope exceeding a threshold of 0.02 along the up-wave transect through time.

5.3.2 Model Domain Setup

Phase-resolved validation of Wavecast requires that the TRIAXYS is contained within the model domain. From Figure 25 (b), it is determined that data within ranges 400 and 1500 meters should be assimilated. The azimuths chosen for assimilation need to incorporate waves travelling towards the radar. The TRIAXYS is at a location where the radar is looking along-crest. Thus, the wave information at least +/- 30 degrees surrounding the TRIAXYS do not contain adequate wave information for assimilation. The domain must be large enough azimuthally to incorporate both incoming waves and the TRIAXYS location. Using these constraints, the grid configured for Wavecast is shown in Figure 26. The assimilation domain outlined in white occupies ranges of 600 m – 2200 m, and azimuths of angles 199 to 325 degrees. The computation domain outlined in black occupies ranges of 100 m to 2200 m and the same azimuths. The sponge layer is 300 meters inside of the initial and final ranges, and 5 degrees inside of the initial and final azimuths, indicated with a red dashed line.

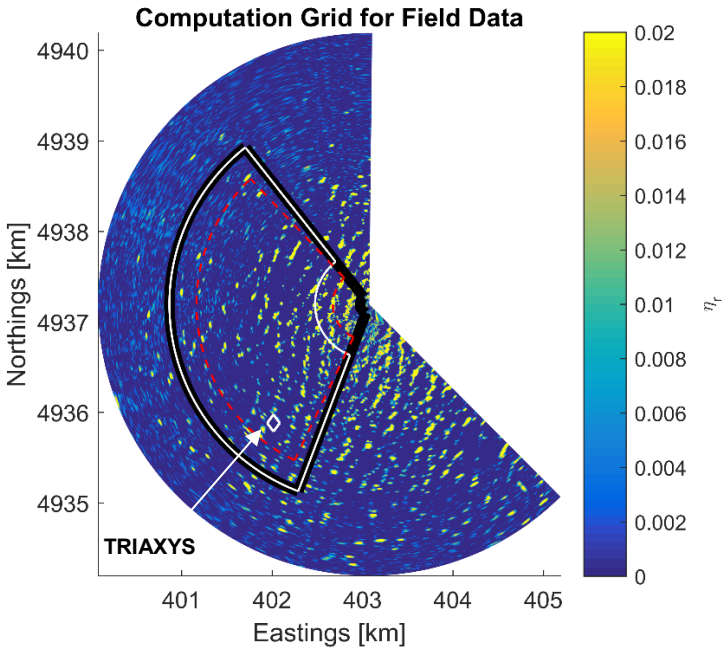

Figure 26. Schematic of Wavecast Model Domain for Field Data.

5.4 Results from Wavecast

Results from eight trials are summarized in

Table 5. The best trial for wave height reconstruction is Umatilla1, in which the frequencies specified correspond to the two peaks in the TRIAXYS spectrum. This trial is repeated in Umatilla2 with a reduced assimilation and prediction time, yielding some reduction in performance. For the remaining trials, only the number and values of the frequencies were changed, as computation time during model testing is not a constraint. Trials Umatilla3 and Umatilla4 use single frequencies at the 20.8 second and 11.1 second peaks, respectively. Using the 20.8 second peak alone in Umatilla3 gives poor results, but using the 11.1 second peak alone in Umatilla4 gives adequate results. Umatilla5 repeats Umatilla1 but with two higher frequencies added. Interestingly, the cost function in Umatilla5 is the lowest, indicating the best match between model and observational data. This may be because two additional source functions are determined, contributing more of the spectrum that will be propagating at the correct phase speed. However, the wave height reconstruction is not as high in Umatilla5 as Umatilla1. Trials Umatilla6, Umatilla7 and Umatilla8 use frequencies chosen from a spectrum made using radar data. Umatilla6 uses two frequencies and shows similar results to Umatilla1. Umatilla7 uses four higher frequencies but excludes the 22 second peak visible in the radar spectrum. Umatilla8 uses the same four frequencies at Umatilla7 but includes the 22 second peak.

Table 5. Summary of Field Trials

Run Name	Cost	Assimilation/Prediction	Num. Freqs.	Freqs (rad/s)	Periods (s)	% H Reconstructed
Umatilla1	0.86	400/400	2	0.3026, 0.5644	20.8, 11.1	44.74
Umatilla2	0.88	200/200	2	0.3026, 0.5644	20.8, 11.1	38.6
Umatilla3	0.988	400/400	1	0.3026	20.8	21.88
Umatilla4	0.8737	400/400	1	0.5644	11.1	33.77
Umatilla5	0.812	400/400	4	0.3026, 0.5644, 0.71, 0.8262	20.8, 11.1, 8.8, 7.6	38.09
Umatilla6	0.857	400/400	2	0.2848, 0.6203	22.1, 10.1	39.9
Umatilla7	0.8743	400/400	5	0.6616, 0.5814, 0.7823, 0.5414, 0.9425	9.9, 10.8, 8.0, 11.6, 6.7	31.51
Umatilla8	0.8394	400/400	6	0.6616, 0.5814, 0.7823, 0.5414, 0.9425, 0.2848	9.9, 10.8, 8.0, 11.6, 6.7, 22.1	34.42

The significant wave height map from the best trial, Umatilla1, is shown in Figure 27 (a). The time series at the GPS coordinates for the TRIAXYS at 1900 UTC is extracted from the domain, and the frequency spectrum is computed. This is shown with comparison to the TRIAXYS frequency spectrum in Figure 27 (b). The significant wave height is reconstructed up to 44.7 %. This is the highest reconstruction value of the Umatilla trials. However, the shape of the Wavecast spectrum does not match the TRIAXYS spectrum at all frequencies. In the Wavecast spectrum, the 20 second and 11.1 second swells do not show up in peaks as distinct as the TRIAXYS spectrum.

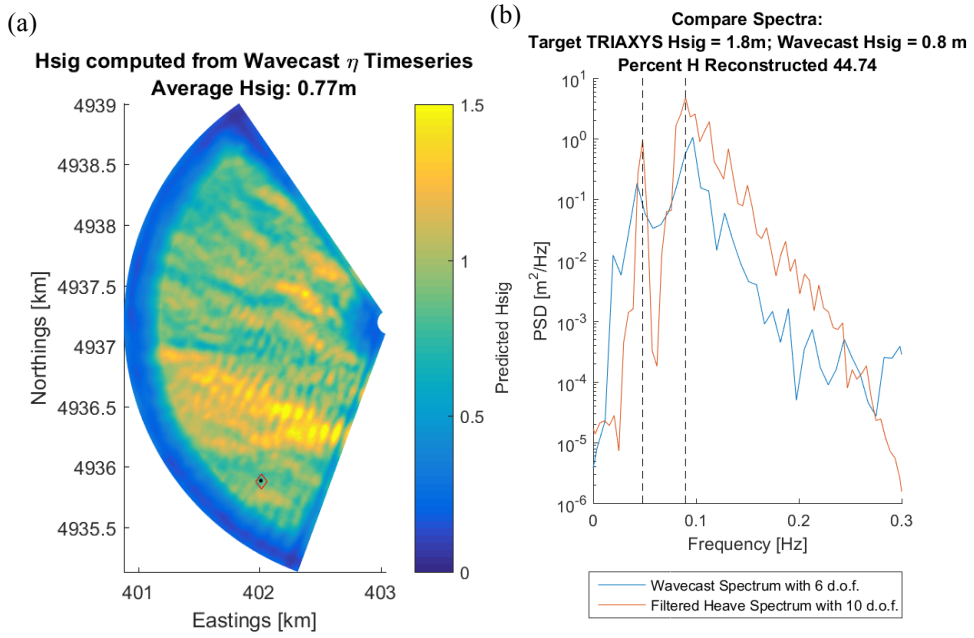

Figure 27. Results from Umatilla1: (a) map of significant wave height and (b) comparison of model and TRIAXYS spectra.

Due to the uncertainties in TRIAXYS and corner marker buoy locations discussed previously, the GPS coordinates provided by the TRIAXYS at the start of data collection are likely not the same coordinates represented in the Wavecast domain. A spatial correlation scheme is developed that looks for the locations of maximum correlation between individual Wavecast time series and the TRIAXYS time series. An annulus of approximately 450m x 20° surrounding the GPS coordinates of the TRIAXYS is chosen for correlations; this domain is shown as a black patch in Figure 28 (a). At each grid point in this annulus, the model time series is cross correlated with the TRIAXYS time series. This yields a correlation value at each lag between the time series. The lag with the highest correlation is plotted at each grid point. Thus, the regions of highest correlation value show the locations with the highest potential correlation between TRIAXYS and model, including the potential for a time lag. Using the 450m x 20° annulus, the correlation map is shown in Figure 28 (b). Interestingly, a swath of high correlation exists parallel to the wave direction. In this annulus of high correlation, the absolute maximum lies at the point specified by a white dot, which is 256 meters from the specified TRIAXYS GPS coordinates. This distance is outside the bounds of uncertainty we expect. However, there are patches of high correlation closer to the TRIAXYS coordinates. The correlation scheme is repeated using a 200m x 7° patch, shown in Figure 28 (c). The maximum peak, shown in Figure 28 (d) is 75 m from the TRIAXYS GPS coordinates, which is closer to the 65 m uncertainty anticipated.

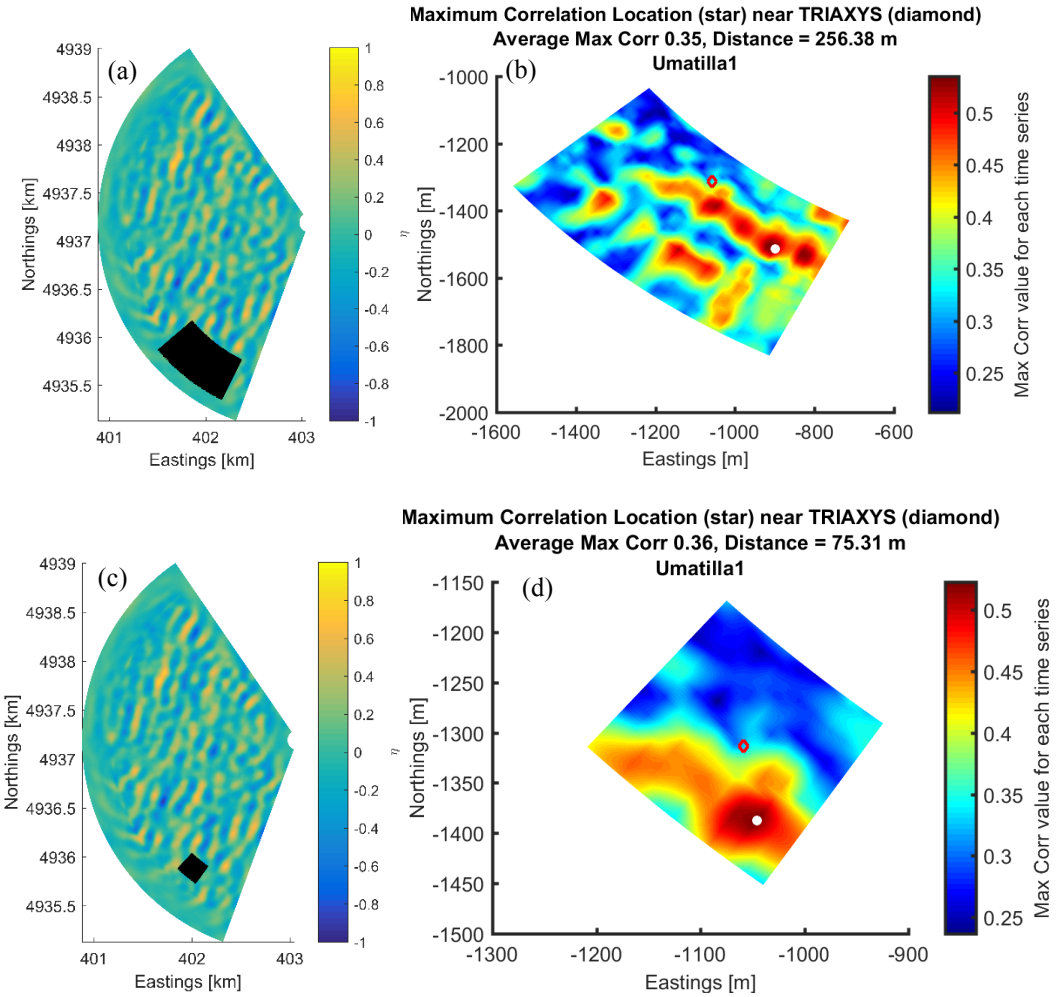

Figure 28. Umatilla1 time series correlation maps: (a) 450m x 20° annulus patch location, (b) correlation map from the (a) patch, (c) 200m x 7° annulus patch location, (d) correlation map from the (c) patch.

The time series at the location of maximum correlation shown in Figure 28 (d) is compared to the filtered TRIAXYS heave in Figure 29. Before applying the lag associated with maximum correlation, the time series are shown in Figure 29 (a). The correlation at each time lag is shown in Figure 29 (b). The maximum correlation occurs with a time lag of 8.7 seconds. Applying this lag, the time series will have maximum correlation, shown in Figure 29 (c). The wave groups appear to align well. Phase agreement is good among a series of waves in the largest wave group.

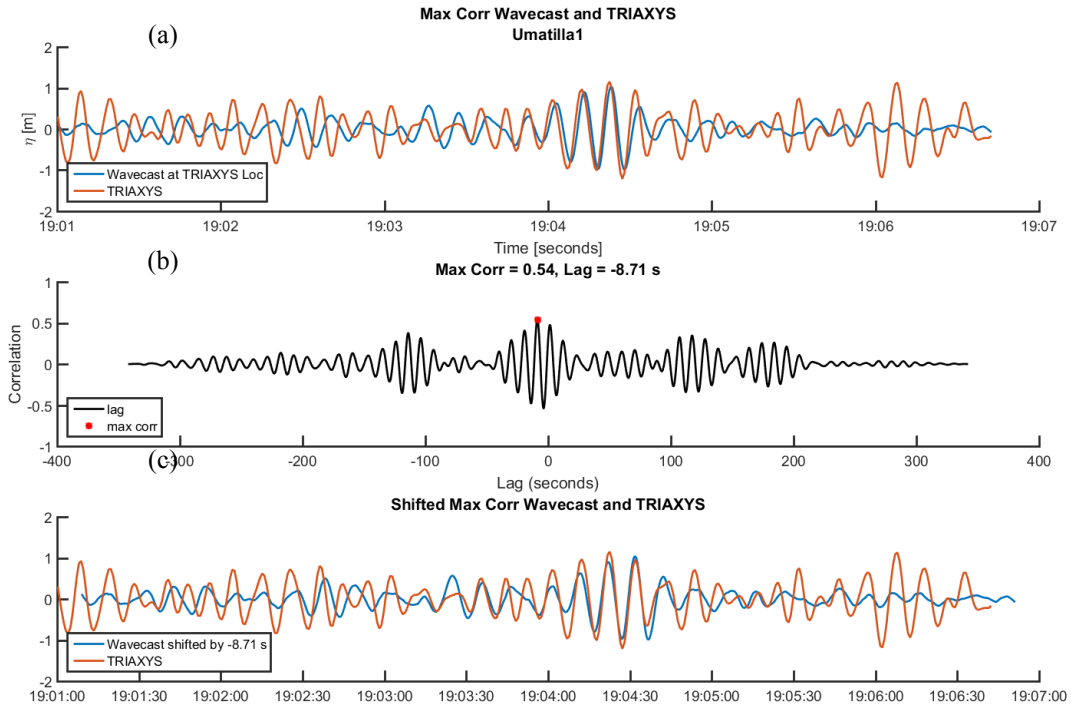

Figure 29. Umatilla1 time series comparison between filtered TRIAXYS heave and the model location of maximum correlation.

6. Filtering the Source Function

All of the waves in a given source function will propagate at the speed of that source function's chosen frequency. This is because the set of MSEs solves for the source function's water surface elevation and velocity potential on a per-frequency basis. In the previous model testing, each source function was filtered using a bandwidth fixed at the same size as the input frequency. In a more recent version of Wavecast, this filtering bandwidth becomes a definable parameter. In this section, a set of trials will be discussed that reduce the size of frequency filtering from 100% to 20%. Using a narrower filtering bandwidth reduces the number of frequency components within the source function, thus reducing the number of frequencies that propagate at the specified frequency. When using the 100% filter, it's likely that the frequencies 50% on either size of the specified frequency are propagating at the wrong speed. This cannot be confirmed without further analysis of the expected phase speeds for each frequency component. However, it is hypothesized that reducing the size of the filtering to 20% will improve the phase comparison between input and model waves.

6.1 Filtering the Synthetic Trials

Filtering was first applied to three synthetic trials, summarized in Table 6. The first filtered trial, Synthetic7, uses the same conditions as the best-case trial using 100% filtering, Synthetic1. Only one frequency is specified. The wave height reconstruction is reduced, as is expected because a smaller portion of the energy spectrum is being used in the source function. The phase agreement does not seem to change by much at the first 3 locations, however there is an improvement at location 4 within the prediction region of the domain. This trial is discussed in more detail below. Two additional trials are summarized, each using two frequencies. The first, Synthetic8, uses two frequencies spaced on the outer edges of the peak frequency. Interestingly, using two frequencies, the wave height reconstruction is poor, only 22 %. However, when the frequencies are spaced closer together, the reconstruction is improved. When looking at the spectrum from Synthetic8, there is a deep notch in the spectrum at the frequency exactly midway between the two specified frequencies. In Synthetic9, the frequency bandwidths have a larger overlap, and the wave height reconstruction is better. The cause of this remains unclear.

Table 6. Summary of Filtered Synthetic Trials

Run Name	Cost	Assim./ Predict.	Num. freqs.	Freqs. (rad/s)	Filtering Bandwidths (rad/s)	Periods (s)	% H Recons-tructed	Correlation at 0 lag			
								Loc. 1	Loc. 2	Loc. 3	Loc. 4
Synthetic7	0.8449	400/400	1	0.6283	0.12566	10	74.52	0.61	0.64	0.54	0.2
Synthetic8	0.9531	400/400	2	0.56549, 0.83503	0.113, 0.167	11.1, 7.5	22.74	0.3	0.48	0.32	0.27
Synthetic9	0.7866	400/400	2	0.5783, 0.7	0.11566, 0.14	10.8, 8.9759	66.96	0.5	0.66	0.48	0.21

Synthetic7 is a filtered version of the best run from the 100% filtered cases, Synthetic1. Recall that this trial uses a single frequency specified at 0.1 Hz. The 20% filter will span frequencies from 0.09 Hz to 1.1 Hz. It is likely that the frequencies at the outer edges of this band are propagating with similar phase speed to the 0.1 Hz component. A map of significant wave height is shown in Figure 30 (a) and the spectra comparison is shown in Figure 30 (b). The wave height reconstruction in trial Synthetic7 is 74.52 %, reduced from 83.03% in Synthetic1. It is seen that the Wavecast spectrum is narrower than in Synthetic1 due to the narrowed filtering.

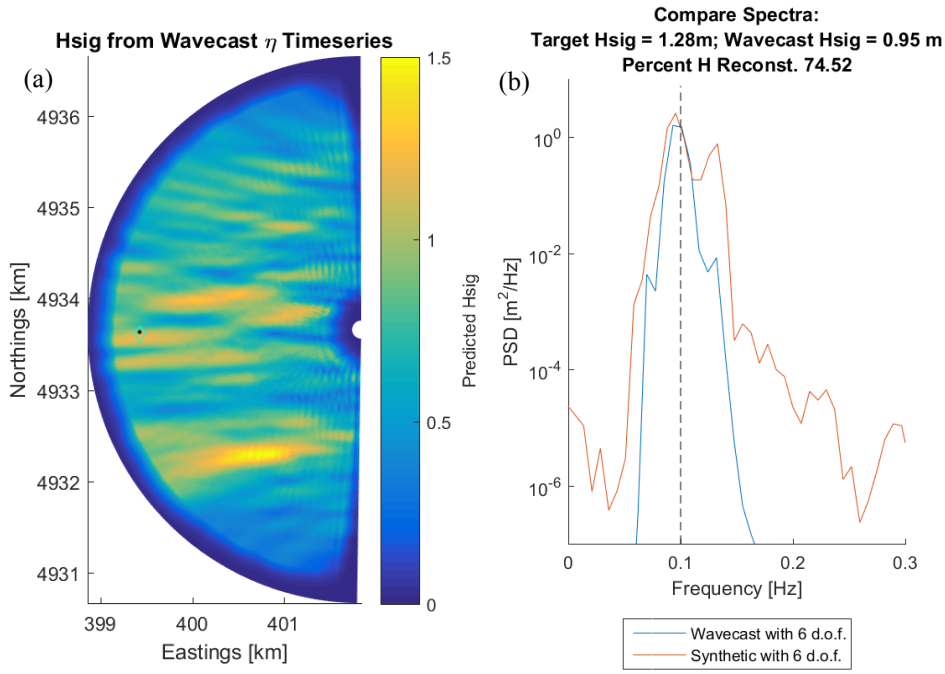

Figure 30. Results from Synthetic7: (a) map of significant wave height and (b) comparison of spectra.

A time series comparison at each of the four locations indicated in Figure 10 is shown in Figure 31. The correlation at locations 1-3 is good, and comparable to Synthetic1. There is some improvement in the correlation at location 4 from Synthetic1. This may be an indication that the reduced bandwidth size improves the accuracy of the phase speeds by reducing the number of frequency components propagated at the incorrect phase speed.

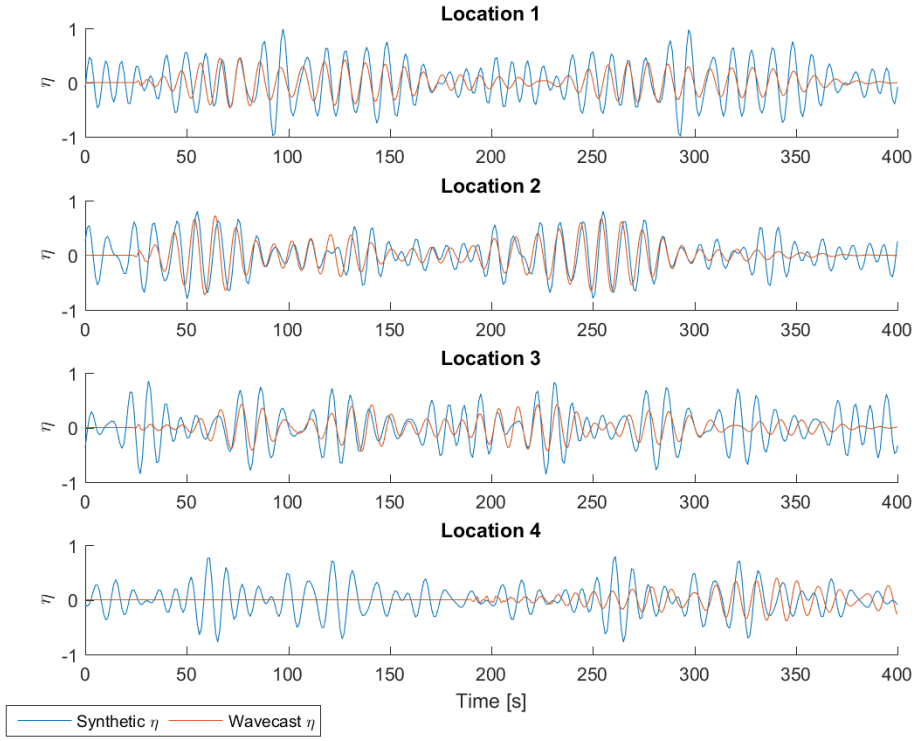

Figure 31. Comparison of water surface elevation at four locations throughout the Wavecast model domain for filtered synthetic testing trial Synthetic7.

6.2 Filtering the Field Trials

The 20% frequency bandwidth filtering is also applied to several Umatilla cases, summarized in Table 7. First, a trial was run using only the 11.1 s swell, thus repeating trial Umatilla4 but with filtering applied. The results show a reconstructed wave height of 22.8%, reduced from 33.7% in Umatilla4. Next, the 20 s swell was added to create trial Umatilla10. This shows an improvement in the wave height reconstruction, and a reduction in the cost function. This trial is the same as Umatilla1 but with filtering, and is discussed in more detail below. The third trial presented is Umatilla11, which has two higher frequencies added. The wave height reconstruction is worsened from the two frequency trial Umatilla11. A reason for this has not yet been found.

Table 7. Summary of Filtered Field Trials

Run Name	Cost	Avg. Max Correlation	Assimilation/ Prediction	Num. freqs.	Freqs. (rad/s)	Filtering Bandwidths (rad/s)	Periods (s)	% H Reconstructed
Umatilla9	0.9285	0.36	400/400	1	0.5644	0.1128	11.1	22.8
Umatilla10	0.8984	0.3	400/400	2	0.3026, 0.5644	0.0605, 0.1128	20.8, 11.1	41.59
Umatilla11	0.8522	0.32	400/400	4	0.3026, 0.564400, 0.75398, 0.942470	0.060520, 0.112880, 0.1508, 0.188500	20.8, 11.1, 8.34, 6.67	38.06

The best field trial using 20% frequency bandwidth filtering is Umatilla10. The map of significant wave height is shown in Figure 32 (a) and spectra comparison in Figure 32 (b). The wave heights are reconstructed up to 41% of the TRIAXYS spectrum, which is only slightly reduced from 44% in Umatilla1. It is also important to note that the Wavecast spectrum from this 20% filtered case is a much better fit in shape to the TRIAXYS spectrum than the 100% filtered case, which was presented in Figure 27 (b). The peaks span the same frequencies as the TRIAXYS spectrum. This is an improvement over Umatilla1.

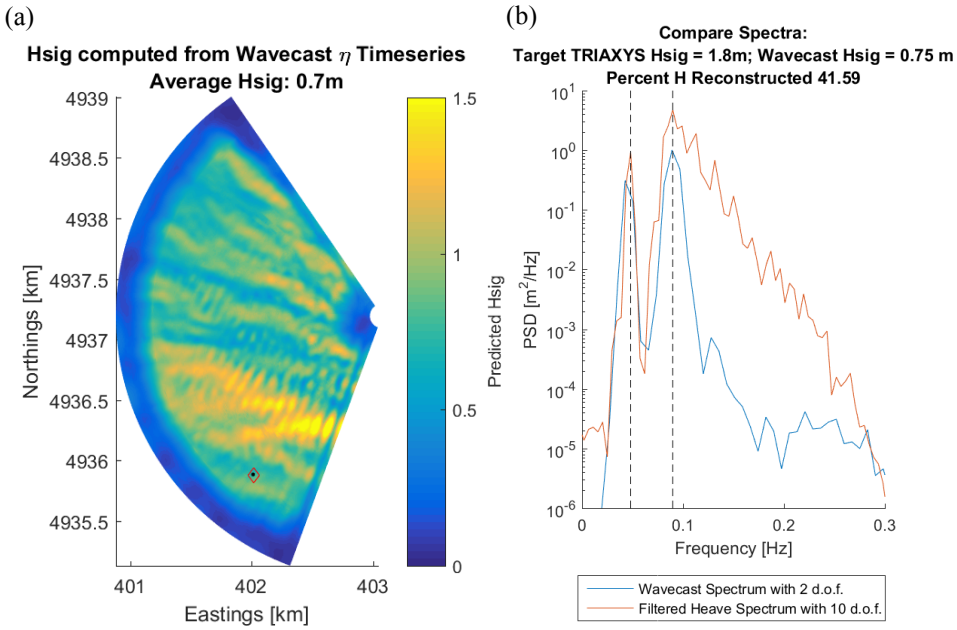

Figure 32. Results from Umatilla10: (a) map of significant wave height and (b) comparison of model and TRIAXYS spectra.

The time series of cross correlation was also carried out in the filtered case. The 200m x 7° cross correlation annulus is presented in Figure 33. The location of maximum correlation is 77.54 m from the recorded TRIAXYS GPS coordinates. This location is not the same as the location of maximum correlation from Umatilla1. However, it is along a similar azimuth. The difference in phase speed due to the reduced size in frequency filtering may account for this.

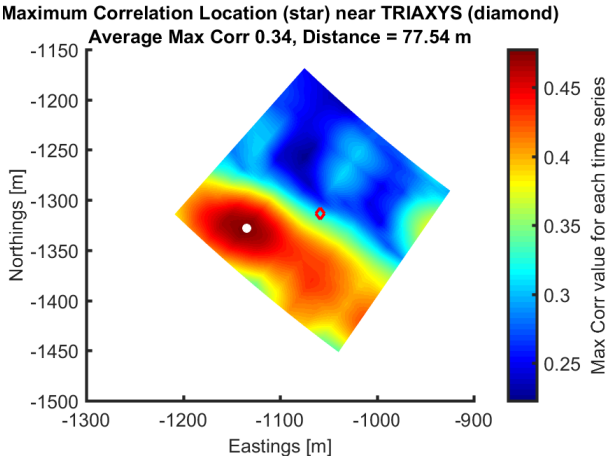

Figure 33. Annulus of maximum cross correlation values from trial Umatilla10.

The raw time series at the location of maximum correlation, indicated by a white dot in Figure 33, is compared to the TRIAXYS time series in Figure 34 (a). The correlation values at each time lag is shown in Figure 34 (a) with the maximum correlation indicated by a red star. The time lag associated with this maximum correlation is applied to the Wavecast time series, and compared to the TRIAXYS time series, shown in Figure 34 (c). This represents the best correlation of time series within the annulus.

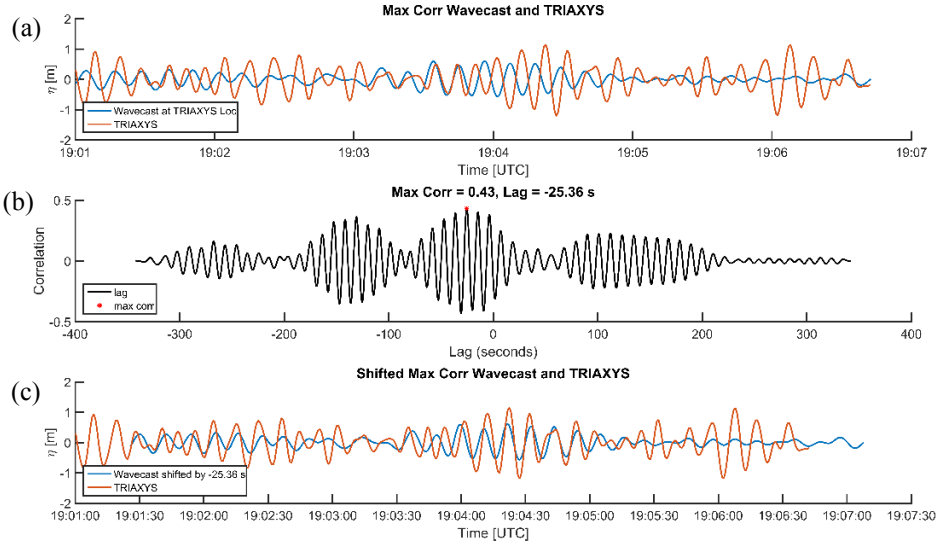

Figure 34. (a) comparison of raw time series at the location of maximum potential correlation, (b) Correlation at each lag value, (c) comparison of TRIAXYS time series and Wavecast time series shifted with lag giving maximum correlation.

7. Forecasting in Real-Time

For implementation of the system as a forecasting technique, a key requirement is that model computation is faster than real time. This section will provide a brief discussion of the constraints in the model that must be considered for forecasting applications.

To make a forecast at the origin of the polar domain, the computation time in Wavecast must not exceed the propagation time of the actual waves. In other words, the waves must be computed at the location of interest before they arrive. The total computation time can be broken into three components: (1) Radar data to be used for assimilation is collected, T_{obs}, (2) The source function is estimated, T_{est}, and (3) The prediction of the waves across the domain is computed, T_{pred}. The sum of these three components must not exceed the time it takes for the observed waves to travel across the total range distance of the domain, $T_{transit}$. This is expressed in equation form by:

$$T_{obs} + T_{est} + T_{pred} < T_{transit}$$

An additional constraint is that combined timing of steps 2 and 3, estimation and prediction, must not exceed the duration of data assimilation. This is to enable concatenation of forecasts. The estimation and prediction steps must be completed before beginning the estimation and prediction using the proceeding assimilation period. This is expressed as:

$$T_{est} + T_{pred} < T_{obs}$$

Finally, the forecast duration possible, T_f, takes into account the actual propagation of the waves across the domain, expressed as:

$$T_f = T_{transit} - (T_{obs} + T_{est} + T_{pred})$$

The transit time can be estimated using knowledge of the total range distance of the domain, R_{domain}, and the phase speed of the dominant wave period,

$$T_{transit} = \frac{R_{domain}}{L_{dom}/T_{dom}}$$

For the model validation attempts described in this study, maintaining real-time computation in each model configuration was not considered. Rather, the aim so far has been on providing the most accurate forecast possible.

8. Conclusions

The presented thesis work outlines the initial testing of a recently developed wave-by-wave forecasting system called Wavecast. The system uses assimilation of radial slope data computed from radar images. The radial slope is the component of the surface slope in the radar look direction, determined using the recently derived Radar Model (Lyzenga & Walker, 2015). From a polar annulus of assimilated radial slopes, Wavecast uses minimization of a cost function to determine the best-fit source function to reconstruct the waves it sees. A source function is determined for each frequency solution to the Mild Slope Equation (MSE) wave model. The final source function is a combination of the source function for each frequency, and is propagated from the outer edge of the assimilation annulus, across a larger polar computation domain towards to origin. When the propagated waves are computed faster than the actual waves arrive, a forecast is made.

The first stage of Wavecast validation uses a synthetic radial slope dataset determined from both a simple monochromatic simulation and a Boussinesq water surface simulation, which bypass the need for the Radar Model. Results of monochromatic testing show strong spectral correlation, and time series correlation of 0.9 throughout the full domain. Results of nonlinear testing show up to 83% spectral correlation of significant wave height, time series correlation up to 0.9 among reconstructed waves, but some decay in correlation among predicted waves. Two causes of this decay in correlation accuracy exist. First, the source function is unconstrained in the frequencies it contains, but all of these frequencies must propagate at the phase and group speed of the specified frequency. Thus, frequency components within the source function that are not the specified frequency may be propagating at the wrong speed. A method for filtering the source function is presented, which may help to correct for this inaccuracy. The second cause of accuracy decay in predicted waves may be due to the discrepancy in wave physics between the wave model and the input wave dataset. Wavecast is formulated using the linear Mild Slope Equation, and the input dataset uses a nonlinear Bousinesq simulation.

The second stage of Wavecast validation uses field data collected from a ship-mounted radar off the coast of Newport, OR. From the field testing, the coupled Radar Model and Wavecast shows the ability to reconstruct wave heights up to 44%. The reduction in reconstructed wave height from the synthetic testing is largely due to the accuracy of the wave data extracted from the Radar Model. For time series comparison, water surface elevation data were collected using a TRIAXYS directional wave buoy within the radar domain. To overcome uncertainty in the location of the TRIAXYS within the model domain, a cross correlation analysis points to the locations of highest correlation between recorded and modeled surface elevation. From model runs with 2-4 specified frequencies, the time series at the location of maximum correlation gives a correlation to the TRIAXYS of up to 0.5 when the time lag is applied. The filtering on the source functions is set to 100% of the specified frequencies for these run, which allows a considerable portion of the spectrum to propagate at an incorrect phase speed.

Initial testing of Wavecast inspired a second version of the system to be produced, where the filtering on the source functions becomes a changeable parameter. Reducing the filtering from 100% to 20% shows similar correlation at locations within the assimilation region, but does provide some improvement at locations outside of the assimilation region where waves are being predicted. In the field testing, the reduced filtering gives a more accurate reconstruction of the frequencies present in the model spectrum. Phase comparison at the location of maximum correlation is comparable to previous trials.

Lessons learned throughout this thesis show encouraging potential of the assimilation algorithm. Additionally, it is shown that radial slope values computed from the Radar Model provide assimilation data that is capable of reconstructing the actual wave spectrum.

References

Belmont, M. R., Baker, J., & Horwood, J. M. K. (2003). Avoidance of phase shift errors in short term deterministic sea wave prediction. *Journal of Marine Engineering & Technology*, *2*(2), 21–26. http://doi.org/10.1080/20464177.2011.11020251

Belmont, M. R., Christmas, J., Dannenberg, J., Hilmer, T., Duncan, J., Duncan, J. M., & Ferrier, B. (2014). An examination of the feasibility of linear deterministic sea wave prediction in multidirectional seas using wave profiling radar: Theory, simulation, and sea trials. *Journal of Atmospheric and Oceanic Technology*, *31*(7), 1601–1614. http://doi.org/10.1175/JTECH-D-13-00170.1

Belmont, M. R., Horwood, J. M. K., Thurley, R. W. F., & Baker, J. (2006). Filters for linear sea-wave prediction. *Ocean Engineering*, *33*(17-18), 2332–2351. http://doi.org/10.1016/j.oceaneng.2005.11.011

Belmont, M. R., Horwood, J. M. K., Thurley, R. W. F., & Baker, J. (2008). Shallow angle wave profiling LIDAR. *Proceedings of the IEEE Working Conference on Current Measurement Technology*, 217–223. http://doi.org/10.1109/CCM.2008.4480871

Berkhoff, J. C. W. (1972). Computation of combined refraction-diffraction. In *Proc. 13th Coastal Eng. Conf.* (pp. 471–490). Vancouver.

Blondel, E., Ducrozet, G., Bonnefoy, F., & Ferrant, P. (2008). Deterministic reconstruction and prediction of non-linear wave systems. *23rd Int. Workshop on Water Waves and Floating Bodies*.

Borge, J. C. N., Reichert, K., & Dittmer, J. (1999). Use of nautical radar as a wave monitoring instrument. *Coastal Engineering*, *37*(3-4), 331–342. http://doi.org/10.1016/S0378-3839(99)00032-0

Borge, J. C. N., Rodríquez Rodríguez, G., Hessner, K., & González, P. I. (2004). Inversion of marine radar images for surface wave analysis. *Journal of Atmospheric and Oceanic Technology*, *21*(8), 1291–1300. http://doi.org/10.1175/1520-0426(2004)021<1291:IOMRIF>2.0.CO;2

Brekken, T. K. (2011). On Model Predictive Control for a point absorber Wave Energy Converter. *Proceedings of the IEEE Trondheim PowerTech*, 1–8. http://doi.org/10.1109/PTC.2011.6019367

Budal, K., & Falnes, J. (1982). Wave power conversion by point absorbers: A Norwegian project. *International Journal of Ambient Energy*, *3*(2), 59–67.

Dankert, H., & Rosenthal, W. (2004). Ocean surface determination from X-band radar-image sequences. *Journal of Geophysical Research C: Oceans*, *109*(4), 1–11. http://doi.org/10.1029/2003JC002130

Fusco, F., & Ringwood, J. (2010a). A study on Short-Term Wave Forecasting for time-domain Control of Wave Energy Converters. *IEEE Transactions on Sustainable Energy*, *1*(2), 99–106.

Fusco, F., & Ringwood, J. V. (2010b). Short-term wave forecasting with ar models in real-time optimal control of wave energy converters. *IEEE International Symposium on Industrial Electronics*, 2475–2480. http://doi.org/10.1109/ISIE.2010.5637714

Fusco, F., & Ringwood, J. V. (2012). A study of the prediction requirements in real-time control of wave energy converters. *IEEE Transactions on Sustainable Energy*, *3*(1), 176–184. http://doi.org/10.1109/TSTE.2011.2170226

Halliday, J. R., Dorrell, D. G., & Wood, A. R. (2011). An application of the Fast Fourier Transform to the short-term prediction of sea wave behaviour. *Renewable Energy*, *36*(6), 1685–1692. http://doi.org/10.1016/j.renene.2010.11.035

Ijima, T., Takahashi, T., & Sasaki, H. (1964). Application of Radars to Wave Observations. In *Proceedings of the 11th Conference of Coastal Engineering 30(1)* (pp. 10–22).

Janssen, T. T., Van Dongeren, A. R., & Kuiper, C. (2001). Phase resolving analysis of multidirection wave trains. In *Ocean Wave Measurement and Analysis, Proc., 4th Int. Symp. Waves* (pp. 377–386). San Francisco, California. http://doi.org/10.1017/CBO9781107415324.004

Li, G., Weiss, G., Mueller, M., Townley, S., & Belmont, M. R. (2012). Wave energy converter control by wave prediction and dynamic programming. *Renewable Energy*, *48*, 392–403. http://doi.org/10.1016/j.renene.2012.05.003

Lyzenga, D. R., & Walker, D. T. (2015). A Simple Model for Marine Radar Images of the Ocean Surface. *IEEE Geoscience and Remote Sensing Letters*, *12*(12), 2389–2392.

Naaijen, P., & Wijaya, A. P. (2014). Phase Resolved Wave Prediction from Synthetic Radar Images. In *Proceedings of the ASME 2014 33rd International Conference on Ocean, Offshore and Arctic Engineering* (pp. 1–9). San Francisco, California.

Nwogu, O. (1993). Alternative Form of Boussinesq Equations for Nearshore Wave Propagation. *Journal of Waterway, Port, Coastal, and Ocean Engineering*, *119*(6), 618–638. http://doi.org/10.1061/(ASCE)0733-950X(1993)119:6(618)

Peregrine, D. H. (1967). Long waves on a beach. *Journal of Fluid Mechanics*, *27*(04), 815–827.

Qi, Y., Xiao, W., & Yue, D. K. P. (2016). Phase-Resolved Wave Field Simulation Calibration of Sea Surface Reconstruction Using Noncoherent Marine Radar. *Journal of Atmospheric and Oceanic Technology*, *33*(6), 1135–1149. http://doi.org/10.1175/JTECH-D-15-0130.1

Schoen, M. P., Hals, J., & Moan, T. (2011). Wave prediction and robust control of heaving wave energy devices for irregular waves. *IEEE Transactions on Energy Conversion*, *26*(2), 627–638. http://doi.org/10.1109/TEC.2010.2101075

Senet, C. M., Seemann, J., & Ziemer, F. (2001). The near-surface current velocity determined from image sequences of the sea surface. *IEEE Transactions on Geoscience and Remote Sensing*, *39*(3), 492–505. http://doi.org/10.1109/36.911108

Valenzuela, G. R. (1978). Theories for the interaction of electromagnetic and oceanic waves - A review. *Boundary-Layer Meteorology*, *13*, 61–85.

Wei, G., & Kirby, J. T. (1995). Tine-Dependent Numerical Code for Extended Boussinesq Equations. *Journal of Waterway, Port, Coastal and Ocean Engineering*, *121*(5), 251–261.

Wijaya, a. P., Naaijen, P., Andonowati, & Groesen, E. Van. (2015). Reconstruction and future prediction of the sea surface from radar observations. *Ocean Engineering*, *106*, 261–270. http://doi.org/10.1016/j.oceaneng.2015.07.009

Wright, F. F. (1965). Wave Observations by Shipboard Radar. *Ocean Science and Ocean Engineering*, *1*, 506–514.

Wu, G. (2004). Direct Simulation and Deterministic Prediction of Large-scale Nonlinear Ocean Wave-field, (1994), 258.

Young, I. R., Rosenthal, W., & Ziemer, F. (1985). A three-dimensional analysis of marine radar images for the determination of ocean wave directionality and surface currents. *Journal of Geophysical Research*, *90*, 1049–1059. http://doi.org/10.1029/JC090iC01p01049

Zhang, J., Yang, J., Wen, J., Prislin, I., & Hong, K. (1999). Deterministic wave model for short-crested ocean waves: Part I. Theory and numerical scheme. *Applied Ocean Research*, *21*(4), 167–188. http://doi.org/10.1016/S0141-1187(99)00011-5

Ziemer, F., & Gunther, H. (1994). A system to monitor ocean wave fields. In *Proceedings of the Second International Conference on Air-Sea Interaction and Meteorology of the Coastal Zone*. Lisbon, Portugal.

Combined References

Belmont, M. R., Baker, J., & Horwood, J. M. K. (2003). Avoidance of phase shift errors in short term deterministic sea wave prediction. *Journal of Marine Engineering & Technology*, *2*(2), 21–26. http://doi.org/10.1080/20464177.2011.11020251

Belmont, M. R., Christmas, J., Dannenberg, J., Hilmer, T., Duncan, J., Duncan, J. M., & Ferrier, B. (2014). An examination of the feasibility of linear deterministic sea wave prediction in multidirectional seas using wave profiling radar: Theory, simulation, and sea trials. *Journal of Atmospheric and Oceanic Technology*, *31*(7), 1601–1614. http://doi.org/10.1175/JTECH-D-13-00170.1

Belmont, M. R., Horwood, J. M. K., Thurley, R. W. F., & Baker, J. (2006). Filters for linear sea-wave prediction. *Ocean Engineering*, *33*(17-18), 2332–2351. http://doi.org/10.1016/j.oceaneng.2005.11.011

Belmont, M. R., Horwood, J. M. K., Thurley, R. W. F., & Baker, J. (2008). Shallow angle wave profiling LIDAR. *Proceedings of the IEEE Working Conference on Current Measurement Technology*, 217–223. http://doi.org/10.1109/CCM.2008.4480871

Berkhoff, J. C. W. (1972). Computation of combined refraction-diffraction. In *Proc. 13th Coastal Eng. Conf.* (pp. 471–490). Vancouver.

Blondel, E., Ducrozet, G., Bonnefoy, F., & Ferrant, P. (2008). Deterministic reconstruction and prediction of non-linear wave systems. *23rd Int. Workshop on Water Waves and Floating Bodies*.

Borge, J. C. N., Reichert, K., & Dittmer, J. (1999). Use of nautical radar as a wave monitoring instrument. *Coastal Engineering*, *37*(3-4), 331–342. http://doi.org/10.1016/S0378-3839(99)00032-0

Borge, J. C. N., Rodríquez Rodríguez, G., Hessner, K., & González, P. I. (2004). Inversion of marine radar images for surface wave analysis. *Journal of Atmospheric and Oceanic Technology*, *21*(8), 1291–1300. http://doi.org/10.1175/1520-0426(2004)021<1291:IOMRIF>2.0.CO;2

Brekken, T. K. (2011). On Model Predictive Control for a point absorber Wave Energy Converter. *Proceedings of the IEEE Trondheim PowerTech*, 1–8. http://doi.org/10.1109/PTC.2011.6019367

Budal, K., & Falnes, J. (1982). Wave power conversion by point absorbers: A Norwegian project. *International Journal of Ambient Energy*, *3*(2), 59–67.

Dankert, H., & Rosenthal, W. (2004). Ocean surface determination from X-band radar-image sequences. *Journal of Geophysical Research C: Oceans*, *109*(4), 1–11. http://doi.org/10.1029/2003JC002130

Fusco, F., & Ringwood, J. (2010a). A study on Short-Term Wave Forecasting for time-domain Control of Wave Energy Converters. *IEEE Transactions on Sustainable Energy*, *1*(2), 99–106.

Fusco, F., & Ringwood, J. V. (2010b). Short-term wave forecasting with ar models in real-time optimal control of wave energy converters. *IEEE International Symposium on Industrial Electronics*, 2475–2480. http://doi.org/10.1109/ISIE.2010.5637714

Fusco, F., & Ringwood, J. V. (2012). A study of the prediction requirements in real-time control of wave energy converters. *IEEE Transactions on Sustainable Energy*, *3*(1), 176–184. http://doi.org/10.1109/TSTE.2011.2170226

Halliday, J. R., Dorrell, D. G., & Wood, A. R. (2011). An application of the Fast Fourier Transform to the short-term prediction of sea wave behaviour. *Renewable Energy*, *36*(6), 1685–1692. http://doi.org/10.1016/j.renene.2010.11.035

Ijima, T., Takahashi, T., & Sasaki, H. (1964). Application of Radars to Wave Observations. In *Proceedings of the 11th Conference of Coastal Engineering 30(1)* (pp. 10–22).

Janssen, T. T., Van Dongeren, A. R., & Kuiper, C. (2001). Phase resolving analysis of multidirection wave trains. In *Ocean Wave Measurement and Analysis, Proc., 4th Int. Symp. Waves* (pp. 377–386). San Francisco, California. http://doi.org/10.1017/CBO9781107415324.004

Li, G., Weiss, G., Mueller, M., Townley, S., & Belmont, M. R. (2012). Wave energy converter control by wave prediction and dynamic programming. *Renewable Energy*, *48*, 392–403. http://doi.org/10.1016/j.renene.2012.05.003

Lyzenga, D. R., & Walker, D. T. (2015). A Simple Model for Marine Radar Images of the Ocean Surface. *IEEE Geoscience and Remote Sensing Letters*, *12*(12), 2389–2392.

Naaijen, P., & Wijaya, A. P. (2014). Phase Resolved Wave Prediction from Synthetic Radar Images. In *Proceedings of the ASME 2014 33rd International Conference on Ocean, Offshore and Arctic Engineering* (pp. 1–9). San Francisco, California.

Nwogu, O. (1993). Alternative Form of Boussinesq Equations for Nearshore Wave Propagation. *Journal of Waterway, Port, Coastal, and Ocean Engineering*, *119*(6), 618–638. http://doi.org/10.1061/(ASCE)0733-950X(1993)119:6(618)

Peregrine, D. H. (1967). Long waves on a beach. *Journal of Fluid Mechanics*, *27*(04), 815–827.

Qi, Y., Xiao, W., & Yue, D. K. P. (2016). Phase-Resolved Wave Field Simulation Calibration of Sea Surface Reconstruction Using Noncoherent Marine Radar. *Journal of Atmospheric and Oceanic Technology*, *33*(6), 1135–1149. http://doi.org/10.1175/JTECH-D-15-0130.1

Schoen, M. P., Hals, J., & Moan, T. (2011). Wave prediction and robust control of heaving wave energy devices for irregular waves. *IEEE Transactions on Energy Conversion*, *26*(2), 627–638. http://doi.org/10.1109/TEC.2010.2101075

Senet, C. M., Seemann, J., & Ziemer, F. (2001). The near-surface current velocity determined from image sequences of the sea surface. *IEEE Transactions on Geoscience and Remote Sensing*, *39*(3), 492–505. http://doi.org/10.1109/36.911108

Valenzuela, G. R. (1978). Theories for the interaction of electromagnetic and oceanic waves - A review. *Boundary-Layer Meteorology*, *13*, 61–85.

Wei, G., & Kirby, J. T. (1995). Tine-Dependent Numerical Code for Extended Boussinesq Equations. *Journal of Waterway, Port, Coastal and Ocean Engineering*, *121*(5), 251–261.

Wijaya, a. P., Naaijen, P., Andonowati, & Groesen, E. Van. (2015). Reconstruction and future prediction of the sea surface from radar observations. *Ocean Engineering*, *106*, 261–270. http://doi.org/10.1016/j.oceaneng.2015.07.009

Wright, F. F. (1965). Wave Observations by Shipboard Radar. *Ocean Science and Ocean Engineering*, *1*, 506–514.

Wu, G. (2004). Direct Simulation and Deterministic Prediction of Large-scale Nonlinear Ocean Wave-field, (1994), 258.

Young, I. R., Rosenthal, W., & Ziemer, F. (1985). A three-dimensional analysis of marine radar images for the determination of ocean wave directionality and surface currents. *Journal of Geophysical Research*, *90*, 1049–1059. http://doi.org/10.1029/JC090iC01p01049

Zhang, J., Yang, J., Wen, J., Prislin, I., & Hong, K. (1999). Deterministic wave model for short-crested ocean waves: Part I. Theory and numerical scheme. *Applied Ocean Research*, *21*(4), 167–188. http://doi.org/10.1016/S0141-1187(99)00011-5

Ziemer, F., & Gunther, H. (1994). A system to monitor ocean wave fields. In *Proceedings of the Second International Conference on Air-Sea Interaction and Meteorology of the Coastal Zone*. Lisbon, Portugal.